Single Photon Infrared Emission Spectroscopy: A Study of IR Emission from UV Laser Excited PAHs between 3 and 15 μm

D. J. Cook, S. Schlemmer, N. Balucani, D. R. Wagner, J. A. Harrison, B. Steiner, and R. J. Saykally*

Department of Chemistry, University of California, Berkeley, California 94720-1460

Received: July 25, 1997; In Final Form: November 10, 1997

Single-photon infrared emission spectroscopy (SPIRES) has been used to measure emission spectra from polycyclic aromatic hydrocarbons (PAHs). A supersonic free-jet expansion has been used to provide emission spectra of rotationally cold and vibrationally excited naphthalene and benzene. Under these conditions, the observed width of the 3.3-μm (C−H stretch) band resembles the bandwidths observed in experiments in which emission is observed from naphthalene with higher rotational energy. To obtain complete coverage of IR wavelengths relevant to the unidentified infrared bands (UIRs), UV laser-induced desorption was used to generate gas-phase highly excited PAHs. Lorentzian band shapes were convoluted with the monochromator-slit function in order to determine the widths of PAH emission bands under astrophysically relevant conditions. Bandwidths were also extracted from bands consisting of multiple normal modes blended together. These parameters are grouped according to the functional groups mostly involved in the vibration, and mean bandwidths are obtained. These bandwidths are larger than the widths of the corresponding UIR bands. However, when the comparison is limited to the largest PAHs studied, the bandwidths are slightly smaller than the corresponding UIR bands. These parameters can be used to model emission spectra from PAH cations and cations of larger PAHs, which are better candidate carriers of the UIRs.

I. Introduction

Conclusive identification of the carriers of the interstellar unidentified infrared bands (UIRs) remains a significant problem for astrophysicists interested in the nature of interstellar dust. (For a review see Allamandola et al.[1,2]) These bands are composed of a series of broad features with no apparent underlying structure at 3.29, 6.2, 7.7, 8.7, and 11.2 μm, and are typically observed toward nebulae in which dust clouds are illuminated by ultraviolet light from a nearby star. Since Polycyclic aromatic hydrocarbons (PAHs) were first proposed as carriers of the UIRs,[3] the PAH model of the UIRs has received much scrutiny and has evolved in response to this scrutiny and the availability of new data.

The argument in favor of PAHs being responsible for the UIRs is primarily based upon the similarity between the frequencies of the UIR bands and the IR-active vibrational frequencies typical of PAHs, and also the anticipated stability of PAHs in environments in which UIRs are generated.[2,4,5] Notably, ab initio[6,7] and matrix[1,8−16] studies of PAH cations yield relative intensities that match the UIR observations more closely than do the relative intensities of neutral PAHs. The case for PAH cations gains further credence when the ionizing UV radiation associated with typical UIR sources is taken into account. Such conditions are anticipated to favor a population of PAHs that is mostly ionized in the regions of UIR generation.[5,17,18]

In the PAH model of the UIRs, an isolated PAH molecule absorbs a UV photon. Internal conversion from the initial excited electronic state to the ground electronic state leaves the entire energy of the UV photon distributed among the vibrational modes of the ground electronic state. The molecule then cools through IR emission. The resulting IR emission spectra from these molecules are characterized by broad bands that exhibit both an increasing red shift and bandwidth with increasing vibrational energy. Although the ab initio calculations and matrix-isolation experiments provide valuable data regarding the frequencies and intensities of PAH cations, they do not provide any information regarding the crucial effects of vibrational energy on the IR emission spectra.

In contrast, studies of gas-phase PAHs with high vibrational energy provide direct measurements of effects of vibrational energy on the IR spectra. FTIR absorption and emission spectroscopy in high-temperature gas cells can be used to probe spectra under equilibrium thermal conditions.[19−21] However, the ultimate temperatures obtainable with thermal-equilibrium measurements are limited by the thermal decomposition of the sample, due primarily to the high-energy tail of the Maxwell−Boltzmann distribution. Furthermore, the bandwidths obtained by such measurements include potential broadening due to rotational contributions. Alternatively, IR emission following pulsed UV laser excitation of gas-phase PAHs can also be measured.[22−26] However, the weak transient signal inherent from this approach, coupled with blackbody radiation from the room-temperature (or hotter) PAH sample cell, has limited these experiments to observation of the 3.3-μm C−H stretching band. Both approaches require generation of gas-phase PAHs under thermal equilibrium conditions, and are limited to readily available neutral PAHs that are easily vaporized. Moreover, thermal equilibrium among vibrational, rotational, and translational degrees of freedom is not thought to occur in the interstellar medium (ISM).

* To whom correspondence should be addressed.

S1089-5639(97)02443-2 CCC: $15.00
Published on Web 02/05/1998

Here we report a detailed account of experiments in which emission from neutral PAHs is observed following UV laser excitation.[26,27] This experimental effort was undertaken in order to determine the characteristic spectroscopic properties of PAHs with high vibrational excitation and to provide more conclusive limitations on the types of PAHs that can and cannot contribute to the UIRs. Two methods were used. In the earlier experiments, which were limited to observation of the 3.3-μm C−H stretching band, either naphthalene or benzene was cooled in a supersonic expansion. A UV laser was then used for excitation, and the resulting IR fluorescence spectrum was measured. In subsequent experiments, IR emission was measured following UV laser desorption of several PAHs. The latter method provides coverage of the entire IR spectral regions corresponding to UIR emission. Both approaches featured the employment of a novel single-photon-counting infrared spectrometer.

In this article, spectroscopic parameters are obtained from the analysis of the single-photon infrared emission spectroscopy (SPIRES) emission spectra. These parameters can be used to model the IR emission spectra from PAH cations for which ab initio or matrix frequencies and intensities are available, as is described in another publication.[28]

II. Experimental Section

A. Single-Photon Infrared-Emission Spectrometer. Emission from gas-phase PAHs following pulsed laser excitation involves detection of a weak transient IR signal. Because Einstein *A* coefficients for spontaneous emission scale with ν^3, typical *A* coefficients for IR emission are small ($\leq 10^3$ s^{-1}) when compared with the values for allowed transitions in the visible and UV ($\leq 10^6$ s^{-1}). Additionally, IR fluorescence is an incoherent process, producing isotropic radiation; owing to solid angle considerations, and conservation of *étendue*, only a small fraction of the light that is produced can be collected and dispersed by a spectrometer. Finally, low number densities are associated with gas-phase samples. These considerations necessitate a highly sensitive detector.

When measurements of weak, transient signals are required in the near-IR through the ultraviolet regions of the spectrum, the detector of choice is the photomultiplier tube, and photon-counting techniques can be employed. When photon counting is possible, the noise associated with the measurement is limited by the statistical fluctuations in the count rate,[29] which is the sum of the photon flux from the incident signal, the background radiation, and the dark count of the device. A novel detector, known as a blocked impurity-band solid-state photomultiplier (BIB-SSPM), has been developed at Rockwell.[30,31] The internal gain mechanism in this As:Si detector is the result of an impurity-band impact-ionization avalanche process. A single incident IR photon is thereby capable of generating a measurable pulse. The development of the BIB-SSPM has made possible a new type of IR spectroscopy, which we call single-photon IR emission spectroscopy (SPIRES). This technique makes use of a BIB-SSPM in conjunction with a liquid-helium-cooled monochromator and photon-counting electronics.

To effectively use the BIB-SSPM, the detector must be cooled to less than 7 K. Additionally, the detector must be shielded from blackbody radiation from the surroundings. Because the BIB-SSPM is capable of efficiently detecting photons from 400 nm to 28 μm and is saturated at count rates near 10^8 s^{-1} cm^{-2}, all optical elements in the field of view of the detector must generate a negligible blackbody photon flux over this range of wavelengths. Therefore, the entire detector environment must be maintained at temperatures lower than 15 K, and cooling with liquid helium is necessary. If the bandwidth of the detector is limited to wavelengths shorter than 10 μm, liquid nitrogen becomes an acceptable cryogen for the collection optics and sample chamber. However, the detector and its immediate environment, including the spectrometer itself, must still be cooled with liquid helium. Room-temperature blackbody radiation becomes excessive at wavelengths longer than 3 μm. For operation through the mid-IR, room-temperature blackbody radiation must be attenuated by a factor of $\sim 10^{12}$. Therefore, all room-temperature objects must be excluded from the field of view of the detector. For measurements at wavelengths longer than 4 μm, simple baffling is not sufficient; everything in the optical path, including the sample, must be contained in a light-tight cryogenic enclosure.

The SPIRES apparatus consists of a liquid-helium-cooled 0.48-m focal length Czerny−Turner monochromator. The monochromator design is illustrated in Figure 1. Wavelength calibration is achieved through measurement of multiple orders of a helium−neon laser. Wavelength reproducibility is typically 400 ppm. Experimental calibration of the relative spectrometer sensitivity using blackbody sources has been hindered by problems associated with stray light and detector saturation. Calibration curves were calculated using the manufacturer's data for diffraction-grating efficiency and detector quantum efficiency as a function of wavelength. Since the sensitivity varies slowly with wavelength, errors in this calibration are not expected to significantly affect measured line shapes. However, the relative intensities of peaks in different regions of the spectrum (e.g., 3 and 12 μm) are not reliably measured and should be considered to be order-of-magnitude estimates. The intensities of peaks observed in the following regions can be reasonably compared with those other peaks observed in the same region: 3−4, 5−9, and 11−15 μm. As will be discussed later, the stability of the pellet in laser desorption experiments is another consideration for relative intensities of peaks in the same spectral region.

The monochromator is equipped with a turret capable of holding three diffraction gratings. For the experiments reported here, a slit width of 1.5 mm was used. The diffraction gratings and approximate slit-limited bandwidths used to collect the data reported here are listed in Table 1. A more detailed description of the spectrometer is available.[32]

B. Free-Jet Experiments. Ultraviolet excitation of PAHs in a supersonic free-jet expansion can allow the observation of emission from PAHs that are both vibrationally hot and rotationally cold−conditions that mimic the interstellar medium (ISM). (There are many excellent discussions of such applications of supersonic expansions available in the literature.[33−35]) The rotational temperature in a free jet can easily be 15 K or lower. Furthermore, low translational temperature and low number densities obtained downstream in the expansion can lead to low collision rates. If the observation time is sufficiently limited, collision-free conditions can be achieved. Under collision-free conditions, with no unimolecular dissociation, the total angular momentum of a molecule will only change by ± 1 unit following absorption of a photon. If a population of low-*J* molecules absorbs a photon, the end result will still be a population of low-*J* molecules. Therefore, the conditions anticipated to exist in the ISM can be reproduced, and the proposed mechanism for UIR generation by interstellar PAHs can be directly tested.

The SPIRES monochromator was interfaced to a vacuum chamber in which a pulsed nozzle was used to generate a free-jet expansion in which benzene or naphthalene were seeded into argon. This apparatus is illustrated in Figure 2. Extensive

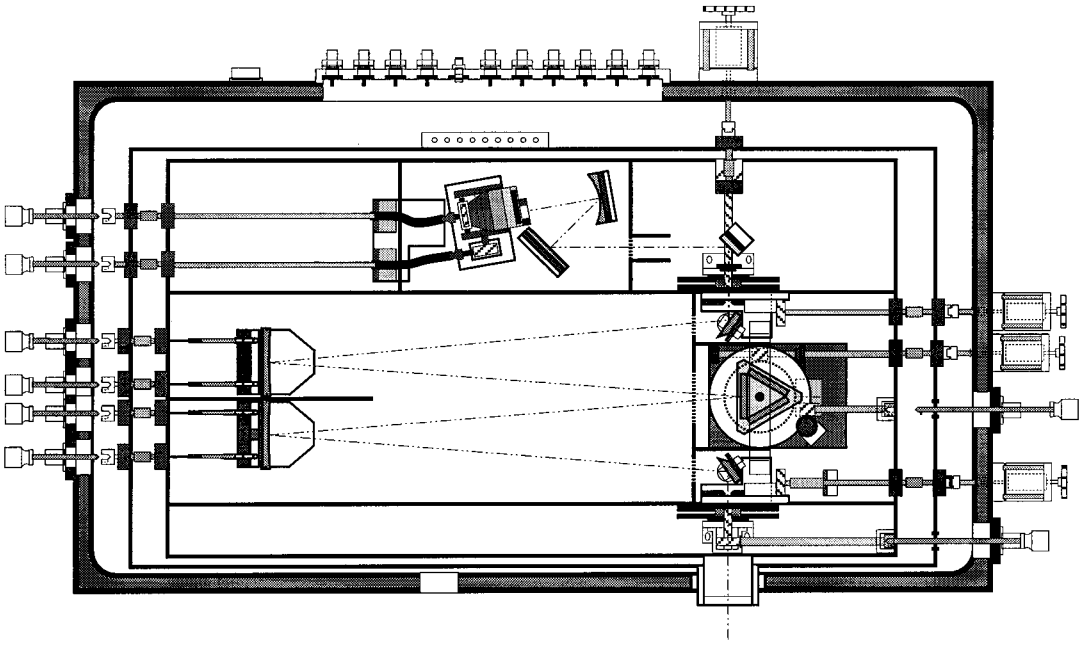

Figure 1. Design of the SPIRES monochromator. The monochromator is housed inside a light-tight liquid-helium-cooled radiation shield and is attached to the bottom of a liquid-helium Dewar. Surrounding the liquid-helium-cooled radiation shield is a liquid-nitrogen-cooled radiation shield, which is in turn enclosed in a vacuum chamber. The Czerny−Turner monochromator consists of two 0.48-m focal length mirrors that collimate the light from the entrance slit to the diffraction grating and that focus the diffracted light onto the exit slit. The diffraction grating is positioned by a turret that is capable of holding three gratings. A heat-switch, which is released before the turret is moved, enables efficient cool-down of the grating turret. Path-folding mirrors are used to direct the light from the slits to the focusing mirrors. Adjacent to the entrance and exit slits are filter wheels; interference filters are used for eliminating higher-order diffraction. Following the exit slit, the light is reflected off two path-folding mirrors, and an ellipsoidal mirror is used to image the vertical exit slit on the vertically oriented 10-element detector array. The detector housing is mounted on a two-axis translation stage. Mechanical feedthroughs are used to couple rotary motion into the monochromator. These feedthroughs are either retractable or heat-sunk on the nitrogen- and helium-cooled radiation shields. The diffraction-grating turret is attached to a worm gear that is driven by a microstepper motor. Once the absolute orientation of the grating is established by measurement of an appropriate diffraction order from a helium−neon laser, the wavelength is determined by counting microstepper motor steps. The signal from each detector element is wired to a preamplifier. These amplifiers employ low-temperature J-FETs which are heat sunk to the liquid-nitrogen-cooled shield.

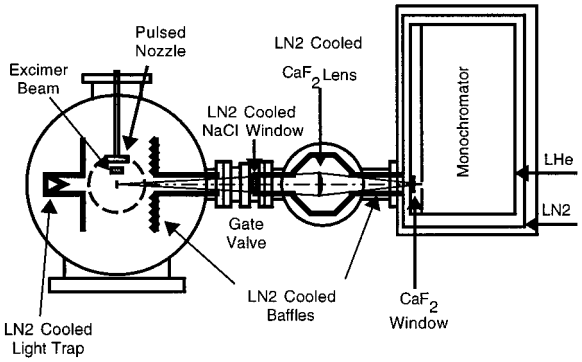

Figure 2. Supersonic free-jet apparatus. A vacuum chamber pumped by a 250-cm (10 in.) diffusion pump is interfaced to the SPIRES monochromator. A pulsed nozzle (General Valve Series 9 with a 1.5-mm orifice) is used to generate a supersonic expansion. Liquid-nitrogen-cooled optical baffling and transfer optics are depicted.

TABLE 1: Configuration of the SPIRES Spectrometer for Collection of PAH Spectra

blaze wavelength (μm)	grooves/mm	approximate useful range (μm)	resolution with 1.5-mm slits (μm)
4	150	2.5−6	0.02
8	75	5−12	0.04
18	50	11−22	0.06

liquid-nitrogen-cooled optical baffling was used in these experiments in order to reduce the blackbody background flux. However, the requirements of pumping the free-jet expansion, and the necessity of a gate valve to separate the monochromator and the expansion chamber, forced the employment of breaks in the shielding. Because of the excessive blackbody background due to these breaks in the baffling, experiments to the red of ~4 μm (2500 cm^{-1}) were not possible, and only emission from the C−H stretching vibrations could be observed in this work.

TABLE 2: Conditions for the Supersonic Free-Jet Expansion[a]

seeded vapor	reservoir temp (K)	nozzle temp (K)	partial pressure seeded vapor (kPa)	pressure at nozzle (P_0) (kPa)
benzene (FJ)	310	390	22	125
benzene (1/4 in.)	285	293−313	6.7	0.024[b]
naphthalene	435	460	24	150

[a] FJ = free jet. 1/4 in. = 1/4-in. nozzle expansion (see text). [b] The pressure at the orifice for the room-temperature source is reduced by the low conductance of the 1/4-in. tubing between the reservoir and the orifice.

Argon carrier gas was seeded with benzene and naphthalene by passing it through a sample reservoir. The temperature dependencies of the vapor pressures of benzene and naphthalene are well-known,[36,37] and the partial pressure of the sample was determined by varying the temperature of the reservoir. Typical conditions for the supersonic expansion are in Table 2.

An excimer laser (Lambda Physik EMG 201 MSC) was used to excite benzene or naphthalene seeded in a supersonic jet. Data were first collected for naphthalene. The 193- and 248-nm excimer lines were used for excitation. Interference from radio frequency noise generated by the excimer discharge necessitated a delay (5−10 μs) between the laser pulse and the observation of emission. The laser intersected the free jet

upstream of the field of view of the monochromator collection optic. The transit time for the molecules to the observation region (40 μs) separated the excimer rf noise from the emission signal when recorded on the multichannel scalar. The distance from the supersonic nozzle to the intersection of the excimer laser was varied in order to investigate possible effects on the spectrum generated by collisions in the free jet. Because of the additional possibility of multiple photon processes, the effects of increasing pulse energy on the spectrum were also monitored.

Spectra of jet-cooled benzene following 193-nm excitation to the S_2 ($^1B_{1u}$) state were also obtained. However, no signal was observed from jet cooled benzene following 248-nm excitation. This was not expected because in previous reports from the literature, 3.3-μm IR emission had been observed from benzene following 248-nm excitation.[23] This discrepancy can be understood if the UV spectrum of benzene is considered. Excitation to the first excited singlet state $^1B_{2u}$ is electronically forbidden, but vibronically allowed. The 248-nm excimer line is on the red tail of the $6_0^1 1_0^2$ band of the $^1B_{2u} \leftarrow {}^1A_{1g}$ transition. In these earlier experiments, the benzene was initially in a room-temperature cell, and under these conditions benzene absorbs 248-nm light.[38,39] When the benzene is jet-cooled, the vibronic band narrows; the band peaks at 247.17 nm, and features primarily on the red side of the peak, which are attributed to hot bands, disappear.[38] There is no longer overlap between the 248-nm laser line and the vibronic transition. To overcome this problem, an expansion from a 6-mm (1/4 in.) nozzle with low backing pressure (estimated to be 0.18 Torr when the conductance of the tubing is considered) was used to generate an approximately room-temperature sample of benzene. Emission spectra were obtained from the room-temperature benzene source at 248 nm with a fluence of 5 MW cm^{-2} and at 193 nm with a fluence of 3.5 MW cm^{-2}.

C. Laser Desorption Experiments. To mitigate the problems with background blackbody radiation, which precluded the measurement of the complete IR spectra with free-jet experiments, a different approach was taken. The method of ultraviolet laser-induced desorption (UV-LID) was used both to introduce PAHs into the gas phase and to simultaneously electronically excite the molecules. This method makes use of a sample Dewar designed to interface with the cryogenic monochromator, which is pictured in Figure 3. In these experiments, a pellet is made by compressing a sample composed of a powdered crystalline PAH with a press. This pellet is mounted on a rotatable cryogenic platform in the sample Dewar. Light from an excimer laser is coupled into the sample Dewar and impinges on the pellet. This generates a plume of desorbed molecules that pass in front of the field of view of the monochromator before being cryopumped onto the walls of the sample Dewar. For experiments at frequencies below 1000 cm^{-1}, the sample Dewar is cooled with liquid helium to reduce blackbody radiation. Liquid nitrogen is an acceptable cryogen for higher-frequency measurements.

The UV-LID technique is not applicable to every PAH that was considered for this work. For some molecules, pellet deterioration was rapid, and it was not possible to obtain reproducible peak intensities. Because this technique is time-consuming and requires significant expenditures for liquid helium, a similar UV-LID apparatus was constructed in which a pellet is mounted on a liquid-nitrogen-cooled coldfinger, and a quadrupole mass spectrometer is used to monitor the laser desorption process. Molecules that did not yield a stable signal were rejected as candidates for the SPIRES experiments. The

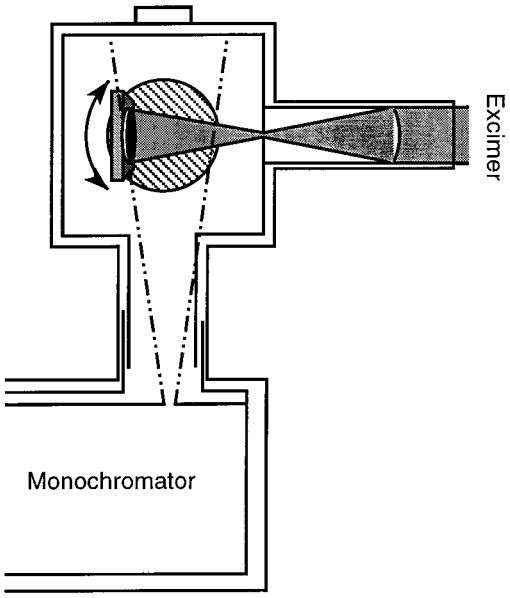

Figure 3. UV-LID apparatus. A PAH pellet is mounted vertically on a rotatable stage. UV radiation from an excimer laser is focused through an aperture in front of the sample and expands to its original fluence before reaching the sample. This reduces blackbody radiation in the sample Dewar and prevents deposition of PAHs onto the UV window. The approximate field of view of the monochromator is depicted with dashed lines. The system of interlocking baffles that allow the retractable sample Dewar to interface with the monochromator is depicted. Not depicted are the bellows, gate valve, and translation stage that are used for retraction of the sample Dewar. Typical excimer-laser fluences range from 1 to 5 MW cm^{-2}. The signal exhibited strong dependence on laser fluence and was also affected by degradation of the pellet due to prior laser pulses. To produce reproducible results, the following procedure was used. A strong peak is first observed in an initial scan. This peak is then used as a reference peak. This peak is measured again, and if a stable signal is observed, this signal is used as a target value. The monochromator wavelength is scanned and 15−20 data points are collected with between 5 and 15 laser pulses per data point. The monochromator is then set to the maximum wavelength of the reference peak, and the signal is recorded. If after a scan the reference signal falls below 80% of the target value, the scan is rejected. The laser power is then increased such that the reference peak signal is no more than 120% of the target value, and the scan is repeated. After a large number of laser pulses (∼1000), observation of a stable signal is no longer possible. Then the sample Dewar must be warmed and vented. The pellet is replaced, or the surface is renewed by scraping with a razor blade.

molecules that were studied are depicted in Figure 4. The mass spectrometer also permitted characterization of potential photofragmentation in the UV-LID process. For many of the molecules, some enhanced fragmentation was observed for UV-LID relative to sources in which PAH vapor was produced by heating in an oven. However, these fragmentation results are ambiguous because it is not clear if this fragmentation occurred in the desorption process, or if the laser desorbed molecules, with high internal energy, were merely more likely to fragment in the electron-bombardment ionizer of the mass spectrometer.

Initially, there was some concern as to whether the observed IR emission was produced by gas-phase molecules or by hot molecules on the surface of the pellet itself. Several observations were made that indicate the emission is indeed generated by laser desorbed gas-phase molecules. First, the orientation of the pellet was varied as pictured in Figure 5. Comparison between the UV-LID signal and reflected light from the pellet surface indicates that the emission does not originate from the surface itself. In another test, a BaF_2 window was placed directly in front of the pellet and 3.3-μm emission following

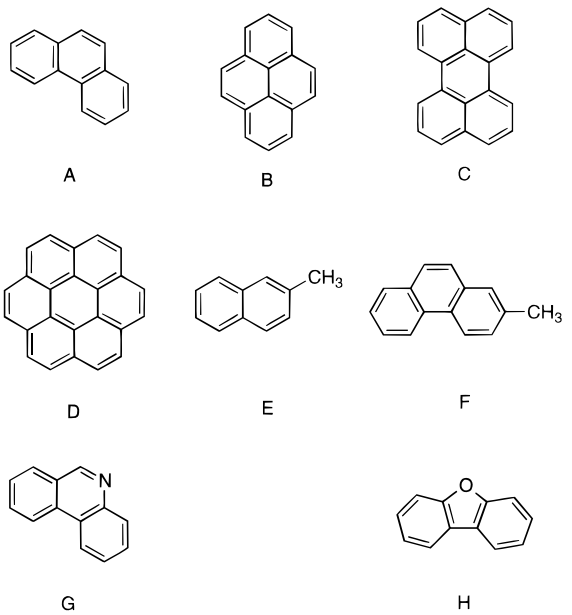

Figure 4. PAHs studied with the UV-LID technique: (A) phenanthrene, (B) pyrene, (C) perylene, (D) coronene, (E) 2-methylnaphthalene, (F) 2-methylphenanthrene, (G) phenanthridine, and (H) dibenzofuran. The following molecules did not generate useful UV-LID data: anthracene, 1,10-phenanthroline, phenazine, and benzo[1,2,3-*bc*:4,5,6-*b′c′*]dicoronene. 9,10-Dihydrophenanthrene generated useful data at 3.3 μm. Although naphthalene generated useful data, the complete spectrum was not obtained.

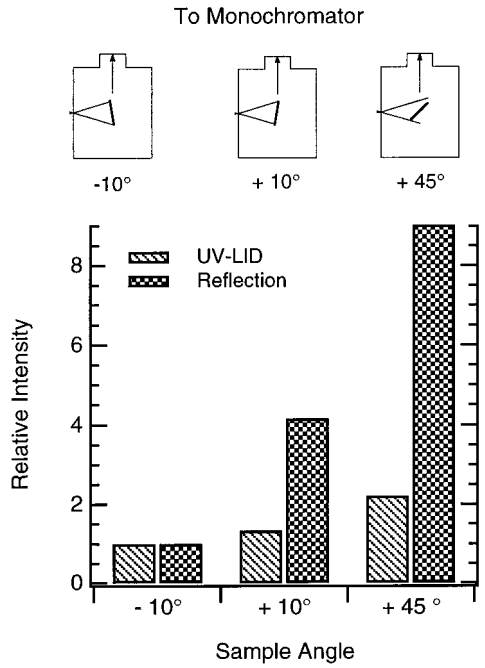

Figure 5. Rotation of the sample to establish emission from a gas-phase carrier. The UV-LID signal is compared with the signal from diffuse reflection of blackbody radiation off the sample surface. If the laser-induced signal were to originate from the surface rather than from the gas-phase material, the dependence upon sample orientation is expected to be similar to that of the illuminated surface. However, only a weak dependence on sample orientation was observed, indicating a gas-phase carrier. (An early configuration is depicted in which the sample holder is not offset from the axis of rotation.)

the laser pulse was monitored. The BaF_2 transmits both the 248-nm excimer radiation and the 3.3-μm emission. However, it blocks desorbed molecules from entering the gas phase. With the BaF_2 window in place, no IR emission was observed.

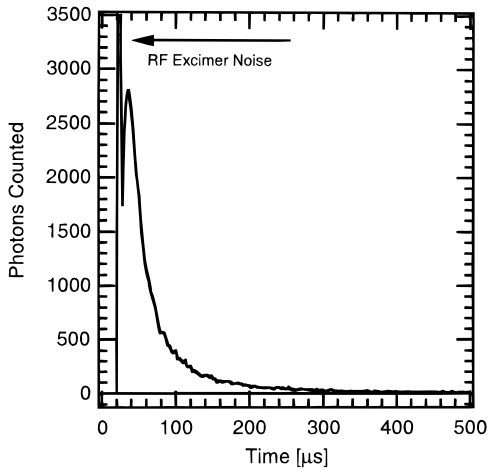

Figure 6. UV-LID time-resolved emission spectra. Emission from perylene was observed at 3.29 μm following 248-nm excitation (500 pulses were averaged). The configuration depicted in Figure 3 was used in which the sample holder is offset from the axis of rotation. The delay between the excimer pulse and observation of a maximum signal is attributed to the time required for the desorbed molecules to travel from the surface to the field of view.

The transient signal observed following the UV absorption also indicates a gas-phase carrier of the emission. A new pellet holder was designed specifically for the UV-LID experiments. The face of this sample holder is offset from the axis of rotation so that the desorbed molecules will more effectively fill the field of view of the monochromator, as pictured in Figure 3. Under these conditions, a distinct rise in signal can be observed following the laser pulse. If the signal were to arise from heating of the surface, a simple decay in the signal is expected. This transient signal is depicted in Figure 6 and provides strong evidence for a gas-phase carrier of the emission.

Additional evidence for a gas-phase carrier of the emission comes from the plume of material that is deposited on the surfaces of the sample Dewar in front of the pellet after experiments have been conducted. This material has similar color, exhibits similar fluorescence, and is also soluble in aromatic solvents such as benzene and toluene, as is the PAH that comprises the pellet. Benzo[1,2,3-*bc*:4,5,6-*b′c′*]dicoronene, which did not produce significant signal, also did not generate a significant plume of condensed material.

III. Results from Free-Jet and Effusive Expansions

A. Naphthalene Free-Jet Results. Spectra of jet-cooled naphthalene obtained following 193-nm (51 800 cm^{-1}) and 248-nm (40 300 cm^{-1}) excitation are displayed in Figure 7. The naphthalene emission spectra exhibit a peak very close to 3.3 μm with a red-degraded line shape. Two modes of approximately equal intensity separated by 11−14 cm^{-1} are expected[6] to provide most of the intensity observed in this band. Because two different laser frequencies were used for excitation, the effects of internal energy can be ascertained. The effects are a red shift, coupled with a broadening of the band. Previous reports[26,24] have attributed the bandwidths and red shifts of the laser-excited bands to a multitude of sequence bands. These highly excited molecules possess multiple quanta of energy distributed among the different modes. Each possible way in which the energy is distributed among these modes constitutes an individual quantum state. If a single quantum transition in one particular mode is observed, excitation in the other modes leads to intermode anharmonicity; each individual quantum state will then have an unique red-shifted frequency. Coupling

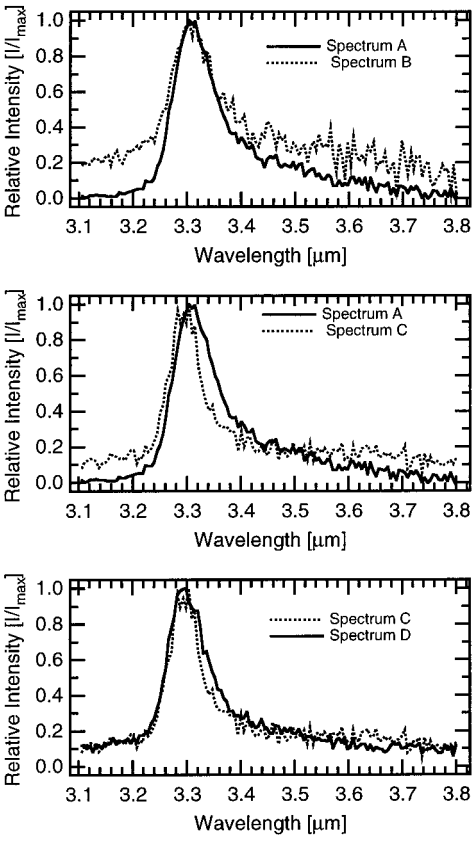

Figure 7. SPIRES data from naphthalene excited in a free jet from which the effects of varying excitation wavelength and nozzle-to-excitation distance (in nozzle diameters, δ) are shown: (spectrum A) 193 nm, 70 mJ, $\delta \approx 20$; (spectrum B) 193 nm, 65 mJ, focused laser; (spectrum C) 248 nm, 190 mJ, $\delta \geq 20$; (spectrum D) 248 nm, 190 mJ, $\delta \approx 2$.

among these states leads to rapid internal vibrational redistribution (IVR) and vibrational dephasing, producing a broadened band with no apparent underlying structure and an increasing red shift with increasing vibrational energy.

Here, the concept of intermode anharmonicity has been introduced. For the subsequent discussion, it will be necessary to differentiate between intermode and intramode anharmonicity. In many vibrational absorption experiments, the transition is between the ground state $|\text{g.s.}\rangle$ and an upper state $|u\rangle$. In a polyatomic molecule, this can be written as follows:

$$|\text{u}\rangle = \begin{Bmatrix} v'_{j=i} = 1 \\ v'_{j\neq i} = 0 \end{Bmatrix} \quad \text{and} \quad |\text{g.s.}\rangle \equiv \{v''_j = 0\}, \forall_j \qquad (1)$$

It is then possible to consider a series of anharmonically shifted transitions arising from states with successively higher quanta in mode i. Here, the upper and lower ($|l\rangle$) states are given by the following expressions

$$|\text{u}\rangle = \begin{Bmatrix} v'_{j=i} = q \\ v'_{j\neq i} = 0 \end{Bmatrix} \quad \text{and} \quad |l\rangle = \begin{Bmatrix} v''_{j=i} = q-1 \\ v''_{j\neq i} = 0 \end{Bmatrix} \qquad (2)$$

Since the anharmonicity is the result of quanta in the mode that is excited by the transition, this is referred to as *intramode* anharmonicity,

Effects of anharmonicity can also be observed when quanta are in modes other than the one that is changed by the transition. This will be called *intermode* anharmonicity to distinguish it from the previously described and more familiar intramode anharmonicity. If a transition in a high-frequency mode i of a small polyatomic molecule is observed, a series of anharmonically shifted bands can be observed due to q quanta in another mode k, which can be sufficiently low in energy to be thermally populated:

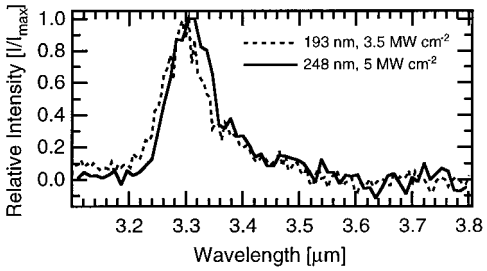

Figure 8. SPIRES data from laser excitation of a room-temperature benzene source.

$$|\text{u}\rangle = \begin{Bmatrix} v'_{j=i} = 1 \\ v'_{j\neq k \text{ or } t} = 0 \\ v'_{j=k} = q \end{Bmatrix} \quad \text{and} \quad |l\rangle = \begin{Bmatrix} v'_{j=i} = 0 \\ v'_{j\neq k \text{ or } i} = 0 \\ v'_{j=k} = q \end{Bmatrix} \qquad (3)$$

If the upper and lower states in a vibrational transition are described by eq 3, a sequence of anharmonically shifted bands can be observed with successively higher values of q. Herzberg has described this phenomenon[40] and referred to the series of transitions shifted by the increasing quanta in mode k as "sequence bands".

In the naphthalene emission spectrum, no distinct sequence of anharmonically shifted transitions is observed. This is expected if the anharmonicities induced by quanta in the various modes (intramode anharmonicity and all different types of intermode anharmonicity) are of the same magnitude. In this case, all the different possible sequences blend together.

Effects attributed to multiple photon processes are also observed when a focused laser is used. Focused excimer lasers are typically efficient at generating photofragmentation if the time scale for internal conversion (often on the order of tens of picoseconds or faster for a polyatomic molecule such as naphthalene) is more rapid than the length of the excimer pulse (typically 10−15 ns). Under such conditions, the cycle of UV absorption followed by rapid internal conversion is repeated. One illustrative example of this mechanism is the 193-nm multiple photon photolysis of C_{60}.[41]

Following the excitation of naphthalene with the focused 193-nm light, 3.3-μm emission is still observed. However, this peak is observed as part of a broad plateau of continuum emission, which extends to the blue of the main feature. The spectra resulting from unfocused 248-nm excitation also show enhanced emission to the blue of the main feature (although not as strong as for the focused 193-nm spectrum). The lower internal energy resulting from the 248-nm photons required higher pulse energies to obtain signal comparable to the signal produced by 193-nm photons. This broad emission to the blue of the main feature in the 248-nm spectra is taken to be an indication of multiple-photon processes incipient at these higher laser fluences.

B. Results for Benzene. SPIRES spectra were obtained from the room-temperature benzene source using 248-nm excitation with a fluence of 5 MW cm^{-2} and also using 193-nm excitation with a fluence of 3.5 MW cm^{-2}. These spectra are displayed in Figure 8. The carrier of the observed emission spectra following 193-nm excitation of benzene is probably not benzene itself. Benzene is known to dissociate upon absorption of a 193-nm photon, and photolysis channels for 193-nm excitation measured under collision-free conditions have been reported by Yokoyama and co-workers.[42]

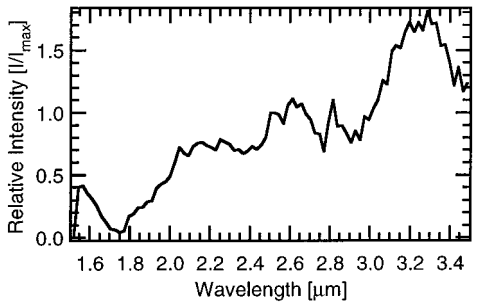

Figure 9. Near-IR SPIRES data for benzene excited at high fluence. Spectra of possible benzene photoproducts following focused 193-nm excitation are shown. Data were obtained in a free-jet expansion at 32 MW cm^{-2}.

The photophysics of benzene following 248-nm excitation are not as clear. Yokoyama et al. have reported H_2 elimination to produce orthobenzyne with a relative branching ratio of 96% following 248-nm excitation of benzene in a skimmed molecular beam; however, absolute quantum yields for 248-nm photolysis were not measured in these experiments. Yerram et al.[43] had difficulty measuring significant 248-nm photolysis under moderately low-pressure conditions. Thermodynamics can assist in determining the carrier of the emission from 248-nm excitation. If single-photon 248-nm excitation is followed by dissociation, the energy available for internal excitation of the orthobenzyne product is quite small. When translational energy release is considered,[42] $\langle E_{\rm Int} \rangle$ is only 3200 cm^{-1}, which must be distributed among the various vibrational modes of the benzene. Therefore, orthobenzyne photoproducts generated by 248-nm excitation are not anticipated to significantly contribute to the observed SPIRES signal. This points to intact benzene molecules as the carrier.

The conclusion that the carriers of the emission differ between 193 and 248 nm excitation helps explain the apparent reversal of the red-shift trends. Although vibrationally hot benzene is observed from 248-nm excitation, 193-nm photolysis produces a different species (primarily phenyl radical[42]), with less internal energy, and the aromatic C−H stretch is observed at a shorter wavelength.

To observe possible multiple-photon effects, near-IR spectra were obtained following excitation of benzene in a free jet with a focused 193-nm laser. These results are displayed in Figure 9. It should be noted that the intensities in Figure 9 have not been corrected for the instrument response. These spectra are presented primarily to provide evidence of near-IR continuum emission resulting from photoproducts of unimolecular benzene decomposition. This near-IR emission is interesting because in addition to the distinct UIR features, a smooth continuum between 1 and 5 μm has been observed in emission from reflection nebulae that exhibit UIR bands.[44] The SPIRES spectra show broad emission from 1.8 to 3.4 μm. Although it is difficult to determine the carrier of the NIR emission, the results of Yokoyama et al.[42] indicate that multiple-photon processes will be significant at the fluences used, and they report many possible photoproducts under these conditions. This raises the interesting possibility that PAH fragments could contribute to this continuum emission, which is sometimes observed along with the distinct 3.3-μm peak in UIR sources.

IV. UV-LID Results

A. Emission-Data Analysis. In the initial reports of this work,[27,26] the UV-LID/SPIRES spectra of the molecules pictured in Figure 4 were presented and compared with the UIR bands.

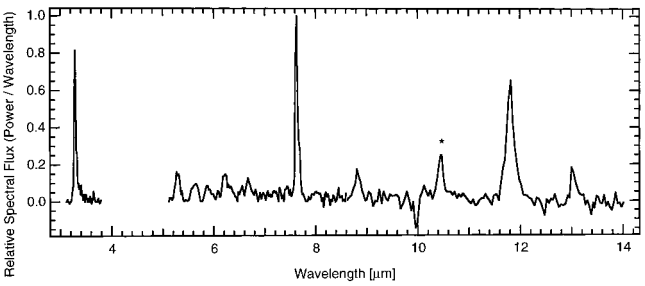

Figure 10. UV-LID/SPIRES spectrum of coronene. The normalized spectral power is plotted vs wavelength. The 10.5-μm peak is a possible contaminant or photolysis product and marked with an asterisk. A plateau that is thought to be an artifact was observed around the 7.6-μm peak and has been subtracted out.

As an example of the results obtained by the UV-LID technique, the spectrum of coronene is presented in Figure 10. For the spectra of all the PAHs studied with the UV-LID/SPIRES method, the reader is referred to our earlier publication.[27] (In the initial publication of UV-LID results,[26] the spectrometer throughput had not been taken into account.) Further analysis of these spectra can provide the characteristic spectral parameters required for modeling emission from candidate carriers of the UIR bands, such as PAH cations and large PAHs, for which gas-phase emission data are not available. The two effects of the high vibrational energy measured in these experiments are a red shift and a broadening of the bands. The bandwidth and the red shift can be extracted from a least-squares fit of a simulated band to the data. Before this can be done, however, the nature of the signal that is measured by the SPIRES spectrometer must be considered in detail.

The photon emission rate Φ_q (with dimensions of photons time^{-1}) generated from an ensemble of emitting molecules is given by

$$\Phi_q = N_u A_{u\rightarrow l} \tag{4}$$

Here, N_u is the population of upper state PAHs and $A_{u\rightarrow l}$ is the Einstein coefficient for spontaneous emission from the upper to lower state. (The subscript q is used to denote radiometric quantities with dimensions of photons, and the subscript e is used to denote radiometric quantities with dimensions of power.) The frequency-dependent signal (with dimensions of photons bandwidth^{-1} time^{-1}) can now be described as

$$\Phi_{q,\nu} = g_\nu(\nu - \nu_0, b_\nu)\Phi_q \tag{5}$$

where ν_0 is the resonant frequency of the transition and b_ν is the bandwidth. (The subscript ν is used to denote spectral radiometric quantities with dimensions of per unit frequency, and the subscript λ is used to denote dimensions of per unit wavelength.) The line shape function (g_ν) is normalized to unity.

The number of photons (N_q) observed by a spectrometer is described by eq 5 folded with the instrument-limited band shape function $s_\nu(\nu)$:

$$N_q(\nu) = N_u A_{u\rightarrow l}\chi_s(\nu) b_{S,\nu} t_{obs} \int_{-\infty}^{\infty} g_\nu(\nu' - \nu_0) s_\nu(\nu' - \nu)\, d\nu' \tag{6}$$

Here, $b_{s,\nu}$ is the spectrometer-limited bandwidth, t_{obs} is the observation time, and $\chi_s(\nu)$ is the frequency-dependent spectrometer throughput, which includes the diffraction-grating efficiency, detector quantum efficiency, miscellaneous optical losses, and the fraction of emitted light that enters the monochromator. s_ν is also normalized to unity. Ideally, the spectrum

should be normalized so that the data represent an intrinsic property of the sample rather than the peculiarities of the instrument. Therefore, it is useful to define the normalized spectral data $\varphi_{q,\nu}(\nu)$ such that

$$\varphi_{q,\nu}(\nu) \equiv \frac{N_q(\nu)}{\chi_s(\nu)\, b_{s,\nu} t_{obs}} \tag{7}$$

With $\varphi_{q,\nu}(\nu)$ defined in this manner,

$$\varphi_{q,\nu}(\nu) = \Phi_q \int_{-\infty}^{\infty} g_\nu(\nu' - \nu_0) s_\nu(\nu' - \nu)\, d\nu' \tag{8}$$

The UIR spectra are typically displayed in units of power per unit wavelength, rather than the photon emission rate per unit frequency. The conversion is given by

$$\varphi_{e,\lambda} = \frac{h\nu^3}{c} \varphi_{q,\nu} \tag{9}$$

The previously published SPIRES spectra[27] were presented as $\varphi_{e,\lambda}$.

Because both $\int_{-\infty}^{\infty} g_\nu(\nu - \nu_0)\, d\nu$ and $\int_{-\infty}^{\infty} s_\nu(\nu - \nu_0)\, d\nu$ are defined such that they are normalized to unity, the integrated band intensities correspond to the product of the excited-state population and the Einstein *A* coefficient:

$$\int_0^{\infty} \varphi_{q,\nu}(\nu)\, d\nu = \Phi_q \tag{10}$$

For a diffraction-grating monochromator with slit-width-limited resolution, the instrument-limited band-shape function is the following triangle function:

$$s_\lambda(\lambda - \lambda_0) = \begin{cases} \dfrac{1}{b_{s,\lambda}^2}(b_{s,\lambda} - |\lambda - \lambda_0|) & |\lambda - \lambda_0| \le b_{s,\lambda} \\ 0 & |\lambda - \lambda_0| > b_{s,\lambda} \end{cases} \tag{11}$$

Here, $b_{s,\nu}$ is defined as the fwhm.

As a result of the high vibrational density of states and intermode anharmonicity, the line shape is theoretically Lorentzian.[45] With the hwhm (half width at half-maximum) given by $b_{L,\nu}$, $g_\nu(\nu)$ takes the familiar form

$$g_\nu(\nu - \nu_0) = \frac{b_{L,\nu}}{\pi} \frac{1}{(\nu - \nu_0)^2 + b_{L,\nu}^2} \tag{12}$$

With these functional forms for both $s_\nu(\nu)$ and $g_\nu(\nu)$, the integral in eq 8 can be evaluated analytically and yields

$$\varphi_{q,\nu}(\nu) = \Phi_q \frac{b_{L,\nu}}{\pi b_{S,\nu}^2}\Big[(a - d)\tan^{-1}(a - d) + (a + d)\tan^{-1}(a + d) - 2a\tan^{-1} a - \frac{1}{2}\ln(x)\Big] \tag{13}$$

$$a = \frac{\nu - \nu_0}{b_{L,\nu}},\ d = \frac{b_{S,\nu}}{b_{L,\nu}},\ \text{and}\ x = 1 + \frac{d^2\,[d^2 - 2(a^2 + 1) + 4]}{(a^2 + 1)^2}$$

It is possible to obtain a least-squares fit of the spectral data to eq 13 using the following four parameters: the instrument-limited bandwidth, the Lorentzian bandwidth, the frequency of the transition (ν_0), and the photon flux from the source. The instrument bandwidth can be fixed at the experimentally measured value (independently determined by measurement of a line from a helium−neon laser), so only three parameters need to be varied for these fits. The approach for obtaining these spectral parameters depends on the availability of ab initio data and whether the band is thought to be the result of a single normal mode or anticipated to be a blended band resulting from multiple normal modes. For coronene, perylene, pyrene, and phenanthrene, the ab initio data from Langhoff is available.[6] For these molecules, most of the observed emission bands can be assigned to one normal mode. These normal-mode assignments are based on the proximity of the observed band to the calculated ab initio frequency. For the most intense bands, these assignments are unambiguous. For some of the weaker bands the assignments are not as clear. In these cases the most probable band was picked on the basis of proximity in frequency and predicted intensity. Only the most intense modes identified by Langhoff were used.[6] These bands were fit to eq 13 using least-squares methods.[46]

The 3.3-μm bands are the result of several multiple normal modes blended together. Therefore, these bands must be modeled as the sum of the *s* individual modes:

$$\varphi_{q,\nu}(\nu) = \sum_{i=1}^{s} \varphi_{q,\nu,i}(\nu) \tag{14}$$

In eq 14, each term arising from an individual mode requires three parameters. Since no distinct bands or shoulders are apparent from these additional modes, eq 14 leads to a surplus of parameters to be fit. To minimize the number of adjustable parameters, the Lorentzian bandwidths of each mode contributing to a blended band are constrained to be equal in value. The ab initio data are used to reduce the adjustable parameters used to describe the intensities. Since these modes are close in energy, the excited-state populations for the modes that contribute to the blended bands are approximately equal. Therefore, the contribution from each mode is expected to be proportional to the relative Einstein coefficients. Only one adjustable parameter for intensity is used, and the relative intensities of the modes that contribute to the band are determined from the ab initio data. A similar strategy is used for the frequencies. The ab initio values are used for each ν_i, and a single adjustable offset is added to the *i* frequencies. In this manner, one adjustable parameter is used for frequency, and the frequency spacings between the modes are constrained to the ab initio values.

B. PAH Frequencies and Bandwidths from UV-LID Data. For those molecules for which ab initio data exist, not every observed band coincides with predicted normal modes. Bands are consistently observed between 5 and 6 μm for which there are no corresponding normal modes. These bands are characteristic of PAHs and are assigned to combination bands. Occasionally, bands are observed at other frequencies that are not easily assigned to normal modes. These could be due either to overtone or combination bands or to the result of impurities generated by photolysis. These bands can also be fit using eq 13. The results of the fits to the coronene, perylene, pyrene, and phenanthrene data are tabulated in Tables 3−6.

For the substituted PAHs, no ab initio data are available. Therefore, the bands from these molecules are treated in the same manner as the unassigned bands for the molecules with ab initio data. If a distinct peak is observed, it is fit to a single mode. If a system of blended peaks is observed, it is fit to multiple bands. In this case, it is not possible to use ab initio data for guidance, and the frequencies and intensities of each band were used as adjustable parameters. Under these conditions, care had to be taken to avoid an excess of free parameters. Therefore, the bandwidths for the modes contributing to blended

TABLE 3: Spectral Parameters from Laser Desorbed Perylene[h]

Simple Bands

		expt				ab initio[a]			
approx λ (μm)	no. of points	fwhm[b] (cm^{-1})	ν_0[c] (cm^{-1})	rel[d] intensity	slit fwhm (cm^{-1})[e]	ν (cm^{-1})	A (s^{-1})	irrep	$\Delta\nu$[f] (cm^{-1})
5.3	13	37.0(9.5)	1893.7(3.0)	8.54(1.4)	14.3				
5.5	9	56(21)	1829.8(4.8)	9.89(2.6)	13.1				
5.7	13	54.5(7.5)	1764.5(2.1)	16.7(1.6)	12.2				
6.7	15	44.2(9.7)	1489.4(2.7)	12.3(1.9)	8.8	1495.3	1.73	B_{2u}	5.9
7.3	19	32.4(2.6)	1371.6(0.83)	25.4(1.4)	7.4	1386.9	8.67	B_{1u}	15.4
7.5	10	26(14)	1326.0(3.6)	6.98(2.6)	7.1	1329.4	1.93	B_{2u}	3.4
8.3	14	21.6(4.7)	1207.0(1.4)	10.0(1.5)	5.8	1216.9	1.08	B_{1u}	9.9
8.5	8	14.8(6.8)	1185.3(1.7)	6.00(1.7)	5.8				
8.7	8	14.4(8.0)	1147.3(20)	5.49(2.0)	5.2				
8.9	11	22.1(7.1)	1122.0(1.8)	10.2(2.3)	5	1134.7	0.659	B_{2u}	12.7
9.3	8	24.3(9.4)	1073.2(2.6)	7.89(2.1)	5	1091.4	0.374	B_{1u}	18.2
9.7	14	45(12)	1028.2(3.2)	13.7(2.7)	4.2	1042.7	0.418	B_{2u}	14.59
10.5	21	45.0(5.3)	955.6(1.5)	27.3(2.3)	5.4	981.8	0.319	B_{3u}	26.2
11.2	15	31(10)	889.7(2.8)	21.4(5.1)	4.7				
12.3	22	14.8(3.2)	808.8(1.1)	77.4(11)	3.9	814.6	9.94	B_{3u}	5.7
13.1	23	16.5(7.6)	762.0(2.6)	100(2)	3.5	765.3	4.61	B_{3u}	3.3

3.3-μm Blended Band

no. of points	Lorentzian fwhm (cm^{-1})	ν_0 (cm^{-1})	$\Delta\nu$ (cm^{-1})	rel intensity	slit fwhm (cm^{-1})
18	23.9(7.6)	3045.0	31.7(2.6)	33(4.0)	18

3.3-μm Blended ab Initio Modes

irrep	ab initio (cm^{-1})	$A_i/\sum_{j=1}^{s} A_j$ [g]	irrep	ab initio (cm^{-1})	$A_i/\sum_{j=1}^{s} A_j$ [g]	irrep	ab initio (cm^{-1})	$A_i/\sum_{j=1}^{s} A_j$ [g]
B_{2u}	3099.27	0.274	B_{2u}	3068.51	0.136	B_{2u}	3048.69	0.0301
B_{1u}	3085.30	0.0350	B_{1u}	3067.57	0.525			

6.3-μm Blended Band

no. of points	Lorentzian fwhm (cm^{-1})	ν_0 (cm^{-1})	$\Delta\nu$ (cm^{-1})	rel intensity	slit fwhm (cm^{-1})
15	38.2(5.7)	1572.4	13.0(1.5)	20.3(1.7)	10

6.3-μm Blended ab Initio Modes

irrep	ab initio (cm^{-1})	$A_i/\sum_{j=1}^{s} A_j$ [g]	irrep	ab initio (cm^{-1})	$A_i/\sum_{j=1}^{s} A_j$ [g]	irrep	ab initio (cm^{-1})	$A_i/\sum_{j=1}^{s} A_j$ [g]
B_{2u}	1596.44	0.225	B_{1u}	1586.01	0.555	B_{1u}	1572.78	0.220

[a] Ab initio data are from Langhoff.[6] [b] $b_{L,\nu}$ from eq 13. [c] ν_0 from eq 13. [d] Φ_q/Φ_{qmax} in percent; Φ_q is from eq 13. [e] $b_{S,\nu}$ from eq 13. [f] $\Delta\nu \equiv \nu_{theory} - \nu_{experiment}$. This is the red shift from the ab initio value. [g] See the text. [h] 95% confidence intervals are in parentheses and are determined from the statistics of the least-squares fit.

systems were constrained to be equal. The results of the fits to the phenanthridine, dibenzofuran, 2-methylnaphthalene, and 2-methylphenanthrene data are presented in Tables 7−10.

Since the absolute throughput of the monochromator is not well-determined, the parameter corresponding to the source photon flux is only a measure of the relative strengths of the bands in any single molecule. Because the efficiency of the laser desorption process varies among molecules, these data do not address differences in intensity among different molecules. In addition, the relative throughput of the monochromator is only approximately determined. Therefore, the information present in the relative intensities is quite limited. To demonstrate that the Lorentzian function best approximates these bands, a comparison of the fit results for Lorentzian and Gaussian band-shape functions is displayed in Figure 11.

C. Temperature of Laser Desorbed Molecules. One significant problem with the laser desorption method is the current lack of quantitative information regarding the internal excitation of the PAHs. In the initial report[26] of the UV-LID measurements, spectra of pyrene and naphthalene up to 7.5 μm were reported. To measure the internal energy, the position of the naphthalene 3.3-μm band from the UV-LID measurements was compared to the positions obtained from the free-jet measurements following 193- and 248-nm excitation. For the free-jet measurements, the initial internal energy is well determined. However, subsequent collisions lead to vibrational cooling, which is expected to be significant, and the extent of this cooling is not well determined. In the initial report of these results,[26] the collisional cooling was neglected, and the internal energy in the molecules was assumed to be equal to the energy of the laser photon. A decrease in energy of 11 500 cm^{-1} between the two laser energies led to a blue shift of the peak from 3021 cm^{-1} following 193-nm excitation to 3039 cm^{-1} following 193-nm excitation. This shift was assumed to be linear with internal energy. From the observed wavelength obtained from the UV-LID measurements, a vibrational energy of ~30 000 cm^{-1} was originally reported.[26] Because collisional cooling was not considered, this calculation probably overestimates the internal energy.

In the case of the larger PAHs, there are no free-jet measurements to use for constraining the internal energy. However, the temperature-dependent red-shift measurements of Joblin et al.[20] obtained from high-temperature equilibrium gas cell emission experiments were available for two of the molecules studied here, coronene and pyrene. Joblin et al. reported the results of fitting the temperature dependence of the frequencies to a line

$$\nu(T) = \nu_0 + \chi T \qquad (15)$$

TABLE 4: Spectral Parameters from Laser Desorbed Phenanthrene

Simple Bands

		expt				ab initio[a]			
approx λ (μm)	no. of points	fwhm[b] (cm^{-1})	ν_0[c] (cm^{-1})	rel[d] intensity	slit fwhm (cm^{-1})[e]	ν (cm^{-1})	A (s^{-1})	irrep	$\Delta\nu$[f] (cm^{-1})
5.3	17	84(11)	1876.4(3.4)	12.3(1.1)	14.1				
5.6	10	81(33)	1779.4(7.6)	13.7(4.2)	12.7				
5.8	7	66(25)	1722.7(7.1)	8.57(2.8)	11.8				
6.1	9	75(23)	1653.5(4.7)	7.63(1.7)	10.7				
6.3	9	69(13)	1583.5(2.4)	6.19(0.86)	10.0	1595.1	1.42	A_1	11.6
6.8	15	80(11)	1476.9(3.6)	16.7(1.9)	8.6	1497.3	1.99	B_2	20.45
8.2	30	68.7(5.5)	1223.8(1.6)	20.5(1.2)	5.9	1250.3	1.84	A_1	26.53
9.8	13	23.2(4.5)	1021.9(1.4)	11.2(1.5)	4.1	1038.3	0.490	B_2	16.41
10.2	9	34.4(7.4)	987.7(1.6)	12.9(2.0)	5.7				
10.7	21	72.0(9.6)	936.4(2.1)	29.7(3.0)	5.2	950.2	0.476	B_1	13.9
11.7	18	48.2(8.8)	851.8(2.2)	32.3(4.6)	4.3	871.4	1.05	B_1	19.6
12.5	30	35.4(2.5)	798.52(0.77)	57.4(2.8)	3.8	817.1	4.99	B_1	18.5
13.8	31	32.0(2.2)	721.66(0.66)	100(4.8)	3.1	736.6	5.07	B_1	14.9

3.3-μm Blended Band

no. of points	Lorentzian fwhm (cm^{-1})	ν_0 (cm^{-1})	$\Delta\nu$ (cm^{-1})	rel intensity	slit fwhm (cm^{-1})
44	90(12)	3036.2	38.1(4.1)	41.0(3.4)	18

3.3-μm Blended ab Initio Modes

irrep	ab initio (cm^{-1})	$A_i/\sum_{j=1}^{s} A_j$[g]	irrep	ab initio (cm^{-1})	$A_i/\sum_{j=1}^{s} A_j$[g]	irrep	ab initio (cm^{-1})	$A_i/\sum_{j=1}^{s} A_j$[g]
A_1	3093.29	0.168	A_1	3063.57	0.235	B_2	3045.76	0.0142
B_2	3082.47	0.184	A_1	3056.99	0.0909	A_1	3045.10	0.0270
A_1	3075.17	0.0136	B_2	3055.41	0.000192	B_2	3041.08	0.00263
B_2	3070.64	0.265						

7.0-μm Blended Band

no. of points	Lorentzian fwhm (cm^{-1})	ν_0 (cm^{-1})	$\Delta\nu$ (cm^{-1})	rel intensity	slit fwhm (cm^{-1})
21	68.8(8.3)	1434.8	23.4(2.4)	18.7(1.6)	8.1

7.0-μm ab Initio Modes

irrep	ab initio (cm^{-1})	$A_i/\sum_{j=1}^{s} A_j$[g]	irrep	ab initio (cm^{-1}	$A_i/\sum_{j=1}^{s} A_j$[g]
B_2	1461.75	0.802	A_1	1443.97	0.198

[a] Ab initio data are from Langhoff.[6] [b] $b_{L,\nu}$ from eq 13. [c] ν_0 from eq 13. [d] $\Phi_q/\Phi_{q\max}$ in percent; Φ_q is from eq 13. [e] $b_{S,\nu}$ from eq 13. [f] $\Delta\nu \equiv \nu_{\text{theory}} - \nu_{\text{experiment}}$. This is the red shift from the ab initio value. [g] See the text.

These results included multiple bands from each of the different molecules studied. Therefore, for both pyrene and coronene, every band with available red-shift data provides an independent measure of the vibrational temperature. The observed frequencies and calculated temperatures for bands with available red-shift data from pyrene and coronene are listed in Tables 11 and 12, respectively.

It is also possible to recalculate the internal-energy estimate for naphthalene using the temperature-dependent red-shift measurements, which were not available when the data were initially published. For the purposes of comparing the temperature of a canonical ensemble to an energy of a microcanonical ensemble, the mean energy can be determined from the vibrational heat capacity. Assuming harmonic oscillators, the vibrational heat capacity for a molecule with s normal modes and with each mode j being m_j-fold degenerate is given by

$$\langle E(T)\rangle = \sum_{j=1}^{s} m_j h\nu_j \left[\exp\left(\frac{h\nu_j}{kT} - 1\right)\right]^{-1} \qquad (16)$$

The vibrational heat capacity of naphthalene is displayed in Figure 12. When the parameters from Joblin et al. for the 3.3-μm band of naphthalene are applied to eq 15, an estimated vibrational temperature of 930 K is the result. From Figure 12, the corresponding mean energy for laser desorbed naphthalene is 12 000 cm^{-1}. In calculating the original estimate of 30 000 cm^{-1}, only two points were available, and it was never clear if a linear extrapolation in energy would be valid over a large range. Since Joblin and co-workers use more than two points to determine the temperature-dependent red shifts, and since the measured frequency is closer to the measurements of Joblin et al., it appears that the red shift might be better described by the relationship of Joblin et al.

D. Comparison of UV-LID to Other Techniques. In addition to the UV-LID method,[26] the naphthalene 3.3-μm C−H stretch has been observed through thermal-equilibrium emission in high-temperature gas cells[19−21] and has also been observed following 193- and 248-nm laser excitation of gas-phase naphthalene—either in thermal equilibrium near room temperature[22−25] or cooled in a free jet (this work). These experiments consistently produce a red-degraded band shape; however, the peak frequency and bandwidth vary from experiment to experiment. As has been mentioned, these parameters appear to depend on internal energy. The bandwidth of the 3.3-μm peak is an important parameter in characterizing the naphthalene spectra, as well as the UIR spectra. Williams and Leone[24] have noted that the bandwidth they obtain from their emission spectra of naphthalene ($\sim$75 cm^{-1}) is larger than the 30 cm^{-1} width of the 3.3-μm UIR band. However, they also note that rotational excitation might contribute to the observed bandwidth. Rotational broadening is also an important concern

TABLE 5: Spectral Parameters from Laser Desorbed Pyrene

Simple Bands

		expt				ab initio[a]			
approx λ (μm)	no. of points	fwhm[b] (cm^{-1})	ν_0[c] (cm^{-1})	rel[d] intensity	slit fwhm (cm^{-1})[e]	ν (cm^{-1})	A (s^{-1})	irrep	$\Delta\nu$[f] (cm^{-1})
5.2	12	33.3(8.3)	1902.9(2.6)	6.93(1.1)	14.7				
5.4	9	31.2(6.7)	1842.1(1.9)	4.03(0.53)	13.6				
5.6	16	45(20)	1771.1(6.0)	10.2(2.9)	12.7				
6.2	11	64(29)	1621.6(8.6)	9.24(3.6)	10.3				
6.3	12	57(15)	1576.9(3.4)	12.4(2.4)	10	1586.1	4.03	B_{1u}	9.2
6.7	13	65(23)	1488.4(5.2)	12.5(3.3)	8.8	1476.2	1.08	B_{2u}	−12
7.0	20	43.7(5.9)	1420.6(1.8)	11.5(1.1)	8.1	1427	3.01	B_{2u}	6.4
8.1	17	37(13)	1230.1(3.4)	10.0(2.4)	6.1	1253.1	0.712	B_{1u}	23
8.5	22	19.0(1.8)	1177.99(0.59)	23.7(1.5)	5.5	1188.3	1.81	B_{2u}	10.3
12.0	46	20.4(1.7)	832.39(0.55)	100(5.6)	2.8	848.3	10.9	B_{3u}	15.9
13.6	37	28(13)	731.0(4.0)	35.0(11.9)	2.1	746.6	0.693	B_{3u}	15.6
14.4	19	32(22)	698.7(5.2)	55.8(29)	1.9	710.9	2.02	B_{3u}	12.16

3.3-μm Blended Band

no. of points	Lorentzian fwhm (cm^{-1})	ν_0 (cm^{-1})	$\Delta\nu$ (cm^{-1})	rel intensity	slit fwhm (cm^{-1})
28	58(11)	3032.1	34.7(3.9)	26.1(3.2)	18

3.3-μm ab Initio Modes

irrep	ab initio (cm^{-1})	$A_i/\sum_{j=1}^{s} A_j$[g]	irrep	ab initio (cm^{-1})	$A_i/\sum_{j=1}^{s} A_j$[g]
B_{1u}	3073.8	0.443	B_{2u}	3053.49	0.106
B_{2u}	3063.24	0.435	B_{1u}	3041.64	0.0161

[a] Ab initio data are from Langhoff.[6] [b] $b_{L,\nu}$ from eq 13. [c] ν_0 from eq 13. [d] $\Phi_q/\Phi_{q\max}$ in percent; Φ_q is from eq 13. [e] $b_{S,\nu}$ from eq 13. [f] $\Delta\nu \equiv \nu_{\text{theory}} - \nu_{\text{experiment}}$. This is the red shift from the ab initio value. [g] See the text.

TABLE 6: Spectral Parameters from Laser Desorbed Coronene

Simple Bands

		expt				ab initio[a]			
approx λ (μm)	no. of points	fwhm[b] (cm^{-1})	ν_0[c] (cm^{-1})	rel[d] intensity	slit fwhm (cm^{-1})[e]	ν (cm^{-1})	A (s^{-1})	irrep	$\Delta\nu$[f] (cm^{-1})
5.3	15	35.5(8.3)	1888.7(2.7)	8.87(1.3)	14.2				
5.6	16	46.5(9.5)	1775.2(2.9)	9.23(1.3)	14				
5.9	13	49(13)	1697.1(3.6)	8.87(1.6)	11.4				
6.2	21	57(13)	1602.3(4.0)	17.6(2.8)	10.3	1602.7	8.45	E_{1u}	0.4
7.6[h]	15	5.3(2.3)	1310.87(0.79)	30.8(5.7)	6.7	1312.4	10.4	E_{1u}	1.6
8.8	18	14.7(2.2)	1132.79(0.73)	15.0(1.5)	5.1	1140.3	2.12	E_{1u}	7.5
10.5[i]	12	8.5(3.2)	956.8(1.1)	26.7(5.7)	5.4				
11.8	22	10.0(1.1)	846.52(0.36)	100(6.5)	4.3	864.4	16.4	A_{2u}	17.9
13.0	14	4.1(3.3)	767.3(1.1)	19.0(7.7)	3.5	774.6	0.878	E_{1u}	7.3

3.3-μm Blended Band

no. of points	Lorentzian fwhm (cm^{-1})	ν_0 (cm^{-1})	$\Delta\nu$ (cm^{-1})	rel intensity	slit fwhm (cm^{-1})
21	24.6(6.6)	3039.2	24.5(2.2)	8.21(1.1)	18

3.3-μm Blended ab Initio Modes

irrep	ab initio (cm^{-1})	$A_i/\sum_{j=1}^{s} A_j$[g]	irrep	ab initio (cm^{-1})	$A_i/\sum_{j=1}^{s} A_j$[g]
E_{1u}	3064.9	0.948	E_{1u}	3042.7	0.052

[a] Ab initio data are from Langhoff.[6] [b] $b_{L,\nu}$ from eq 13. [c] ν_0 from eq 13. [d] $\Phi_q/\Phi_{q\max}$ in percent; Φ_q is from eq 13. [e] $b_{S,\nu}$ from eq 13. [f] $\Delta\nu \equiv \nu_{\text{theory}} - \nu_{\text{experiment}}$. This is the red shift from the ab initio value. [g] See the text. [h] The plateau under the 7.6-μm band was subtracted from the data for the fits. [i] Probably an impurity or a decomposition product.

for the UV-LID experiments, since the rotational temperature is not well defined.

One distinct advantage of the free-jet measurement is the low rotational excitation characteristic of jet-cooled molecules. Free-jet rotational temperatures of ≤15 K are routinely achievable, which are considerably lower than the typical temperature of the dust (∼100 K) in the UIR sources. However, the free-jet experiments have two potential problems. First, they are not entirely collision-free. These collisions can lead to vibrational cooling and also to rotational heating through vibration-to-rotation energy redistribution. In addition, clusters can be formed in the source. If one (or more) of the molecules in a small cluster absorbs a photon, the high vibrational energy in the excited molecule will lead to dissociation of the cluster, and the excited molecule will be liberated. However, it is possible that some energy can be transferred to rotations in the dissociation process. Therefore, rotational excitation is still of some concern in the free-jet experiment.

To ascertain the importance of collisions, experimental and/or theoretical data on collision-induced energy transfer must be available. Although such data is not readily available for naphthalene, they do exist for benzene. In addition to comparing the 3.3-μm emission spectra of laser-excited benzene and naphthalene to the UIRs,[23] Barker and co-workers[43,47,48] have reported measurements of collisional cooling of laser-excited benzene (denoted benzene*) with a either a buffer gas or room-

TABLE 7: Spectral Parameters from Laser Desorbed Dibenzofuran[e]

Simple Bands

approx λ (μm)	no. of points	Lorentzian fwhm[a] (cm^{-1})	ν_0[b] (cm^{-1})	rel[c] intensity	slit fwhm[d] (cm^{-1})
3.3	25	45.8(6.4)	3057.0(2.2)	16.1(1.5)	18
5.7	9	41(19)	1759.7(5.3)	6.23(1.9)	12.2
6.3	15	35.5(2.9)	1573.05(0.94)	14.5(0.77)	10
6.9	31	54.0(4.7)	1443.4(1.6)	59.1(3.0)	8.3
7.7	23	61.6(7.9)	1295.3(2.3)	48.7(4.5)	6.7
8.4	16	25.4(4.5)	1188.6(1.4)	71.8(8.6)	5.6
9.0	21	20.1(2.2)	1107.93(0.71)	26.0(1.9)	4.9
9.9	20	36.3(6.6)	1005.9(2.0)	33.5(4.1)	4.1
10.9	16	29.4(6.1)	919.2(1.8)	15.7(2.3)	5

11.8-μm Blended Band

no. of points	Lorentzian fwhm (cm^{-1})	slit fwhm (cm^{-1})	ν_0 (cm^{-1})	rel intensity
44	20.9(1.8)	4.3	857.9(1.0)	33.1(2.6)
			834.85(0.88)	38.4(2.7)

13.5-μm Blended Band

no. of points	Lorentzian fwhm (cm^{-1})	slit fwhm (cm^{-1})	ν_0 (cm^{-1})	rel intensity
44	24.1(2.8)	3.3	747.3(1.2)	100(8.9)
			720.1(1.6)	69.4(7.4)

[a] $b_{L,\nu}$ from eq 13. [b] ν_0 from eq 13. [c] Φ_q/Φ_{qmax} in percent; Φ_q is from eq 13. [d] $b_{S,\nu}$ from eq 13. [e] 95% confidence intervals are in parentheses and are determined from the statistics of the least-squares fit.

TABLE 8: Spectral Parameters from Laser Desorbed Phenanthridine[e]

Simple Bands

approx λ (μm)	no. of points	Lorentzian fwhm[a] (cm^{-1})	ν_0[b] (cm^{-1})	rel[c] intensity	slit fwhm[d] (cm^{-1})
5.2	8	38(12)	1912.0(3.4)	2.85(5.8)	14.7
5.5	16	108(12)	1800.1(3.3)	10.3(0.87)	13.1
6.0	11	73(20)	1674.7(4.4)	4.86(0.94)	11
6.4	19	65.9(5.1)	1567.5(1.5)	17.2(0.92)	9.7
6.8	7	58(17)	1470.8(3.2)	10.4(2.5)	8.6
7.0	11	48(10)	1432.8(2.5)	11.3(1.7)	8.1
8.1	20	38.7(3.6)	1219.4(1.1)	16.7(1.1)	6.1
9.8	18	23.2(4.0)	1024.1(1.2)	5.12(6.3)	4.1
10.1	9	27.2(9.6)	987.5(2.5)	9.90(2.4)	5.8
10.6	11	43(11)	936.3(2.7)	25.4(5.3)	5.3
11.4	28	51.2(3.4)	873.7(1.0)	32.1(1.6)	4.6
13.6	58	37.9(2.1)	729.97(0.70)	100(3.9)	3.2

3.3-μm Blended Band

no. of points	Lorentzian fwhm (cm^{-1})	slit fwhm (cm^{-1})	ν_0 (cm^{-1})	rel intensity
40	52.0(7.8)	18	3048.3(2.9)	14.3(1.5)
			2979.8(7.7)	5.25(1.1)

[a] $b_{L,\nu}$ from eq 13. [b] ν_0 from eq 13. [c] Φ_q/Φ_{qmax} in percent; Φ_q is from eq 13. [d] $b_{S,\nu}$ from eq 13. [e] 95% confidence intervals are in parentheses and are determined from the statistics of the least-squares fit.

temperature benzene that is not excited. These measurements indicate that after initial absorption of a 248-nm photon, the mean energy transfer per benzene*−benzene collision[47] is 1200 cm^{-1} and the mean energy transfer per benzene*−argon collision[43] is 40 cm^{-1}.

Theoretical investigations of collisional energy transfer for benzene*−benzene[49] and benzene*−argon[50] collisions produce results for the benzene vibrational energy loss that agree with experimental measurements following absorption of a 248-nm photon (1076 and 59 cm^{-1} per collision, respectively). The energy loss for benzene*−argon collisions is anomalously low for a molecule the size of benzene. This is thought to be due to a lack of low-frequency modes in the highly symmetrical molecule. For hexafluorobenzene*−argon collisions, the energy loss per collision is calculated[50] to be 446 cm^{-1}. For toluene*−argon collisions, ∼200 cm^{-1} are lost per collision.[47,51] The energy loss per collision is roughly linear with energy. The numbers reported here are for molecules that are initially at room temperature and absorb a 248-nm photon.

Although the experimental investigations only measure vibrational energy loss, the theoretical calculations help to elucidate the importance of the various energy-transfer channels.

TABLE 9: Spectral Parameters from Laser Desorbed 2-Methylphenanthrene[e]

Simple Bands

approx λ (μm)	no. of points	Lorentzian fwhm[a] (cm^{-1})	ν_0[b] (cm^{-1})	rel[c] intensity	slit fwhm[d] (cm^{-1})
5.4	15	81(14)	1874.0(4.0)	28.5(3.4)	14
5.6	9	113(36)	1778.8(8.7)	36.5(10)	13
5.8	8	70(17)	1728.1(3.3)	28.1(5.0)	12
6.4	11	119(28)	1584.8(4.3)	62.1(12)	10
6.9	25	119(11)	1451.0(2.7)	100(6.9)	8.3
8.1	21	80(12)	1229.1(2.6)	48.3(5.2)	6.1
10.0	37	72(12)	997.8(3.2)	36.2(4.5)	4
11.6	23	41.2(4.6)	864.6(1.3)	30.3(2.4)	4.4
12.6	23	36.0(4.0)	797.6(1.1)	40.0(3.1)	3.8
13.7	45	33.7(5.0)	732.9(1.7)	54.5(5.7)	3.2

3.3-μm Blended Band

no. of points	Lorentzian fwhm (cm^{-1})	slit fwhm (cm^{-1})	$\nu_{0\,(cm^{-1})}$	rel intensity
50	100(11)	18	3030.9(4.7)	67.8(5.8)
			2893.4(7.8)	38.7(4.5)

[a] $b_{L,\nu}$ from eq 13. [b] ν_0 from eq 13. [c] Φ_q/Φ_{qmax} in percent; Φ_q is from eq 13. [d] $b_{S,\nu}$ from eq 13. [e] 95% confidence intervals are in parentheses and are determined from the statistics of the least-squares fit.

TABLE 10: Spectral Parameters from Laser Desorbed 2-Methylnaphthalene[e]

Simple Bands

approx λ (μm)	no. of points	Lorentzian fwhm[a] (cm^{-1})	ν_0[b] (cm^{-1})	rel[c] intensity	slit fwhm[d] (cm^{-1})
5.3	10	61(24)	1898.4(6.7)	4.74(1.3)	14
5.7	14	102(25)	1752.2(5.5)	15.0(2.7)	12
6.2	8	68(20)	1631.0(5.1)	9.05(2.3)	10
6.3	11	76(20)	1587.5(4.3)	15.6(3.1)	10
6.7	9	43(13)	1501.0(3.3)	13.1(2.9)	9
7.3	21	93(11)	1362.9(2.6)	23.7(2.1)	7
10.5	15	45(11)	945.6(2.6)	39.7(6.7)	5.4
11.4	15	61(15)	874.9(4.3)	64.7(14.5)	4.6
11.9	11	37.5(8.4)	841.3(2.4)	68.6(13)	4.2
12.4	22	40.9(3.1)	805.93(0.85)	92.3(5.2)	3.9
13.6	35	36.2(2.6)	732.29(0.80)	100(5.0)	3.2

3.3-μm Blended Band

no. of points	Lorentzian fwhm (cm^{-1})	slit fwhm (cm^{-1})	ν_0 (cm^{-1})	rel intensity
40	41.3(4.2)	18	3050.7(2.0)	10.2(0.81)
			3001.2(4.7)	4.31(0.65)
			2925.3(3.1)	5.97(0.62)
			2871.2 (6.3)	2.68 (0.52)

[a] $b_{L,\nu}$ from eq 13. [b] ν_0 from eq 13. [c] Φ_q/Φ_{qmax} in percent; Φ_q is from eq 13. [d] $b_{S,\nu}$ from eq 13. [e] 95% confidence intervals are in parentheses and are determined from the statistics of the least-squares fit.

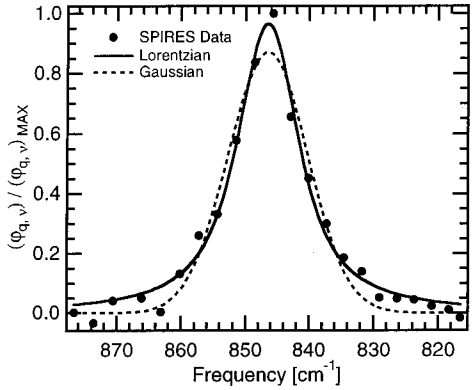

Figure 11. Lorentzian and Gaussian fits to the coronene 11.8-μm A_{2u} band. The appearance of the fits, the residuals, and relative values of χ^2 (0.031 for the Lorentzian fit and 0.064 for the Gaussian fit) indicate the emission band is better described by a Lorentzian function.

TABLE 11: Pyrene Vibrational Temperature from Frequency-Shift Measurements

	high-temp gas cell[20]		UV-LID (this work)	
band (μm)	ν_0 (cm^{-1})	χ ($\times 10^{-2}$ cm^{-1}/K)	ν (cm^{-1})	T (K)
3.3	3062.9	−2.22	3034	1302
8.5	1187.9	−1.00	1179	890
12.0	847.6	−1.69	833	864
			mean temp	1019

TABLE 12: Coronene Vibrational Temperature from Frequency-Shift Measurements

	high-temp gas cell[20]		UV-LID (this work)	
band (μm)	ν_0 (cm^{-1})	χ ($\times 10^{-2}$ cm^{-1}/K)	ν (cm^{-1})	T (K)
3.3	3077.2	−3.52	3041	1028
6.2	1635.1	−4.36	1608	622
7.7	1325.9	−2.38	1311	626
8.8	1141.5	−0.840	1133	1012
11.8	865.0	−2.30	847	782
			mean temp	814

For benzene*−benzene,[49] 947 cm^{-1} of the 1076 cm^{-1} that is lost per collision is accounted for by vibration-to-vibration transfer, 39 cm^{-1} is channeled to rotational energy of the benzene*, 34 cm^{-1} goes to rotational energy of the benzene, and the remaining 57 cm^{-1} goes to translational energy. For benzene* − argon collisions, 26 cm^{-1} of the total 59 cm^{-1} that is lost is partitioned to benzene* rotational energy. These results might lead one to believe that collisional cooling of a vibrationally excited molecule can lead to substantial rotational heating. However, the dominant collision partner in the free jet is translationally cooled argon, and vibration-to-rotation energy transfer is mitigated by the more efficient process of rotation-to-translation energy transfer. In general, these opposing effects will lead to a slightly elevated "quasi-steady-state" rotational temperature.[50]

For the experimental and theoretical studies of benzene collisional cooling,[43,50,51] Lennard-Jones potential parameters were used to calculate Lennard-Jones collision rates.[52] However, the collisional energy-loss parameters for naphthalene are not determined, and the number density and translational temperature must be estimated from the theory of supersonic expansions.[53] The calculations are further complicated by the continuously decreasing collision rate between the location of excitation and the viewing region, which is an additional 17 nozzle diameters downstream. A simple estimate of collision numbers from approximate hard-sphere cross sections and a constant number density yields an estimated 15 naphthalene−naphthalene and 56 naphthalene−argon collisions between excitation and observation, which are upper limits.

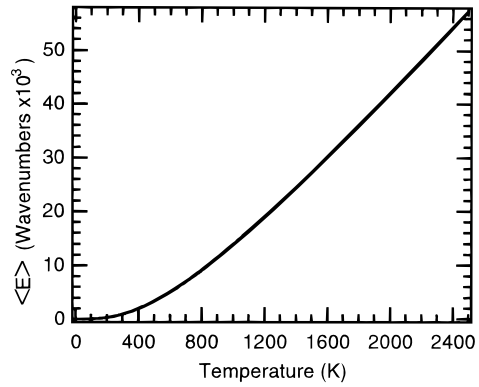

Figure 12. $\langle E_{vib} \rangle$ vs T for naphthalene calculated using eq 16 with ab initio frequencies from Langhoff[6] and assuming harmonic oscillators. This result can be used to compare results of experiments using samples described by a canonical ensemble with results of experiments that are described by a microcanonical ensemble.

TABLE 13: Naphthalene 3.3-μm Bandwidths under Different Excitation Conditions[g]

method	ref	$\langle E_{vib} \rangle$ (cm^{-1})	T_{vib} (K)	apparent fwhm (cm^{-1})	estimated rotational T (K)
LE, FJ	this work	<51800[a]	2320	90	≤100
		<40300[a]	1945	75	≤100
LE, FGC	23	40300[b]	1945	80[c]	∼300
LE, FGC	25	≪51800[d]	2320	80	∼380
LE, FGC	24	<51800[a]	2320	90[e]	∼300
		<40300[a]	1945	80[e]	∼300
UV-LID	this work	∼12000[f]	930	50	
TEA, SGC	20	10750	873	50	873
		2970	473	35	473

[a] Some cooling due to collisions is expected. [b] The collision-free spectrum is extrapolated from data with varying numbers of collisions.[23] [c] Extrapolated from the instrument slit function, as reported by the authors. [d] Considerable cooling due to collisions is expected.[23] [e] Inferred from Figure 3a in the reference. [f] Calculated from temperature-dependent red-shift data.[20] [g] LE = laser excitation. TEA = thermal emission and absorption. FJ = free jet. FGC = flowing gas cell. SGC = static gas cell, and UV-LID = ultraviolet laser-induced-desorption.

Because of the uncertainty in the extent of collisional cooling in the free-jet experiment, the naphthalene internal energy was calculated using the temperature-dependent data of Joblin and co-workers.[20] The results for 193 (51 800 cm^{-1}) and 248 nm (40 300 cm^{-1}) excitation of naphthalene in a free jet are 3070 and 2320 K, respectively. These temperatures correspond to mean internal energies of 75 000 and 52 000 cm^{-1}, respectively (see Figure 12). This calculation obviously overestimates the internal energy of the laser-excited naphthalene. Therefore, it appears that the internal energy in these molecules is significantly greater than the mean energy of the temperatures used by Joblin and co-workers to obtain the temperature-dependent red-shift data, and it appears that these red-shift data of Joblin et al. do not extrapolate well to considerably higher internal energies.

Because there are available naphthalene 3.3-μm data from such a wide variety of experiments, it is possible to compare the bandwidths observed under these conditions and see if any trends are evident. The bandwidth data are therefore displayed in Table 13. From these data, the following trend does emerge. The observed bandwidth clearly depends strongly on vibrational energy, and the rotational temperature does not appear to provide

a major contribution to the bandwidths observed in the laser-excited sources. In the experiments of Shan, Suto and Lee, with relatively high numbers of collisions that are expected to lead to rotational heating and vibrational cooling, the observed bandwidth following 193-nm excitation is narrower than other bandwidths reported following 193-nm excitation. In the experiments of Joblin et al., spectra are measured with relatively low internal energy and high rotational temperature; rotational broadening provides a significant contribution to the observed bandwidths. Even under these conditions, Joblin et al. report observed bandwidths that increase with the first power of T and note that an increase with $T^{1/2}$ would be expected for simple rotational broadening. Therefore, the PAH bandwidths observed by the UV-LID experiments are expected to be primarily broadened by vibrational internal energy.

V. Astrophysical Implications

A. Neutral PAHs Coronene and Smaller. Significant discrepancies between the spectra of the neutral PAHs studied with the UV-LID technique and the UIR bands were been considered in the first report of the UV-LID/SPIRES data,[26] which covered a limited portion of the UIR spectrum and did not include the instrument response function. Discrepancies between these neutral PAH emission spectra and the UIRs remain and have been described in the initial report[27] of the work presented here. These discrepancies are summarized as follows. First, the relative band intensities differ considerably. In the case of the UIRs, the 6.2- and 7.7-μm UIR bands are strong when compared with the 3.3- and 11.2-μm bands; the laboratory PAH spectra exhibit the opposite result.

Second, the frequencies of the bands in the "fingerprint" region of the spectrum (between 6 and 9 μm) corresponding primarily to C−C stretching and C−H in-plane bending vibrations vary considerably among the different PAHs. The UIRs are not postulated to arise from a single molecule. Rather, they are postulated to arise from a family of molecules with similar structure and presumably similar infrared spectra. If a preponderance of the molecules of a particular type generate bands near frequency ν_C, with bandwidths of $\sim\Gamma_C$, then a conglomerate spectrum of several molecules will produce a peak with a bandwidth $\gtrsim\Gamma_C$ at frequency ν_C. Similarly, if the molecules produce an apparently random distribution of peaks over a spectral region wider than Γ_C, then the result will be a broad continuum. Therefore, a peak in the conglomerate spectrum will exhibit high contrast if the individual molecules consistently fail to generate bands at wavelengths at which no features are observed in the conglomerate spectrum. Such consistency from individual PAHs is observed in the case of the 3.3-μm C−H stretching bands.

When the fingerprint region of the UIR spectrum is considered, the 7.7-μm feature is quite broad (70−200 cm^{-1}), and a wide range of frequencies from the individual molecules can, in principle, reproduce this feature. However, the 6.2-μm UIR feature typically has a width of 30 cm^{-1}.[2] To reproduce the structure of the fingerprint region of the UIR spectra, a 6.2-μm feature must be general to these molecules, or at the very least to a subset of these molecules. Additionally, a distinct gap between the 6.2- and 7.7-μm UIR bands is observed. However, this gap typically does not drop to nondetectable levels of emission, and the size and extent of this gap vary among UIR sources. Furthermore, a weak feature at 6.9 μm is observed in some sources.[2,54,55] (This feature can be obscured by a strong Ar II feature in sources with H II regions.) Therefore, although the carriers of the UIRs must, in general, not emit in the gap between the 6.2- and 7.7-μm bands, emission from a small subset of the carriers in this region is certainly tolerated. In fact, a tendency for a subset of the carriers to emit near 6.9 μm, as is observed with small PAHs reported here, is consistent with the PAH-UIR hypothesis.

Transitions between 5 and 6 μm are common for PAHs and are typically assigned to combination bands and/or overtones. Features in the UIR spectra at 5.2 and 5.6 μm have been attributed to these characteristic PAH vibrations.[2,56] Similar emission features are observed in the UV-LID spectra. However, for many of the PAHs reported here, the intensities of these bands are of the same order of the C−C stretching modes between 6 and 8 μm. In the case of the UIR spectra, the 5.2- and 5.6-μm intensities are, respectively, 5% and 7% of the 7.7-μm band.[54]

Although the 3.3-μm UIR band is reproduced quite well by the PAHs studied here, clear discrepancies exist in the fingerprint region of the spectrum and in the C−H bending bands between 11 and 15 μm. Although these discrepancies indicate that small neutral PAHs alone cannot reproduce the UIR spectra, these discrepancies could possibly be resolved if a broader distribution of PAHs is considered.

B. Laboratory Emission Spectra and the 3.3- and 3.4-μm UIR Bands. As previously mentioned, the 3.3-μm bands observed in our spectra do show a remarkable invariance in frequency among the different PAHs studied. Although the PAHs studied are smaller than those implicated by the PAH-UIR hypothesis, the invariance in frequency and band shape of the C−H stretching bands among the studied PAHs is likely to extend to larger PAHs. Furthermore, in the context of the PAH-UIR hypothesis, a broad size distribution is expected; the 3.3-μm emission will be dominated by PAHs on the small side of the PAH size distribution with fewer internal degrees of freedom. Therefore, the strong similarity between the 3.3-μm PAH emission feature and the corresponding UIR band remains an important factor in implicating PAHs as potential carriers of the UIRs. These considerations also make it worthwhile to examine this region of the spectrum more closely.

There has been considerable discussion in the literature[57] that the minor 3.4-μm UIR feature is associated with anharmonically shifted $\upsilon = 1 \leftarrow \upsilon = 2$ transitions in the aromatic C−H stretching modes and that an additional smaller feature to the red is due to transitions arising from $\upsilon = 3$ states (sequence bands arising from intramode anharmonicity). In support of this idea, Brenner and Barker[23] have fit features on the red tail of the benzene emission spectrum following 248-nm excitation to these intramode sequence bands. However, Williams and Leone[24] conclusively demonstrated that similar emission features are not present in emission spectra from gas-phase naphthalene following 193- and 248-nm excitation. The free-jet emission spectra[26] obtained concurrently with and independently of the work of Williams and Leone also provided evidence of a lack of such hot bands. In addition, SPIRES spectra produced by 248-nm excitation of benzene under collision-free conditions, as shown in Figure 8, failed to reproduce the features observed by Brenner and Barker. Finally, none of the UV-LID emission spectra from the unsubstituted PAHs reported in this section show a distinct feature near 3.4 μm. This finding can be simply explained if the intermode anharmonicities are assumed to be of the same magnitude as the intramode anharmonicity. A multitude of anharmonically red-shifted sequence bands blended together can account for the apparently featureless red-shift and red-degraded plateau that is observed in the spectra of the unsubstituted PAHs.

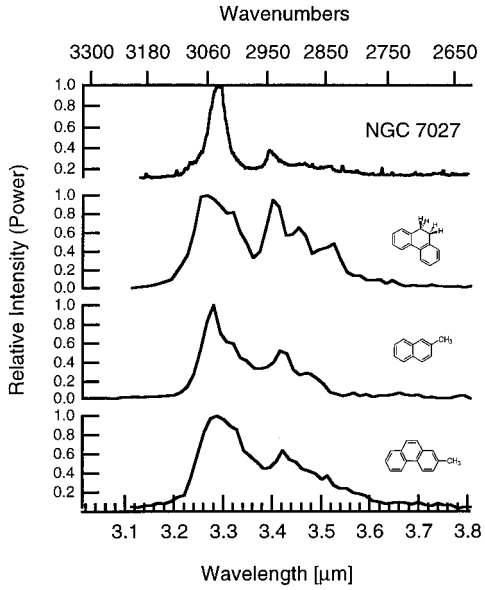

Figure 13. SPIRES spectra of aliphatic-substituted PAHs and NGC 7027.[65] PAHs with aliphatic substitutions can generate bands that resemble the minor 3.4-μm UIR feature.

Aliphatic C−H stretching bands have been postulated as an alternative source of the structure to the red of the primary 3.3-μm UIR band. The 3.4-μm UIR band is in a region of the spectrum where aliphatic C−H stretching is often observed. Although this band does not coincide well with any of the particular frequencies listed by Bellamy[58] for primary, secondary, and tertiary aliphatic C−H sites, it is not always possible to observe distinct peaks for molecules with many different aliphatic groups. Therefore, the assignment of this band to aliphatic hydrogen vibrations is not unreasonable. Because of the possibility that PAHs with aliphatic substitutions could produce the 3.4-μm band, such PAHs were examined in our UV-LID measurements. In Figure 13, the emission spectra from the aliphatic-substituted PAHs studied with the UV-LID/SPIRES method are displayed along with the 3−4 μm emission from the UIR source, NGC 7027. Schutte et al.[59] noted similarities between the spectra of super-hydrogenated PAHs and this portion of the UIR spectra, and the results from the 9,10-dihydrophenanthrene are indeed especially close to the UIR features. The aliphatic-substituted PAHs certainly provide a better match to this portion of the UIR spectrum than the results from the unsubstituted PAHs. It is plausible that the proper mixture of unsubstituted and aliphatic-substituted PAHs could reproduce the 3.29- and 3.4-μm UIR bands. Shan, Suto, and Lee[25] arrived at a similar conclusion after examining the IR emission spectra of unsubstituted and methyl-substituted PAHs following 193-nm excitation.

There are now astrophysical observations that also favor the aliphatic hydrogen hypothesis over the idea of sequence bands arising from intramode anharmonicity. In IRAS 21282 + 5050, a broad emission feature has been observed at 1.68 μm and has been assigned to the two-quantum overtone of the 3.29-μm UIR band.[60] By the difference in the frequencies of these two bands, the $v = 1 \leftarrow v = 2$ transition does not coincide with the 3.4-μm feature. Additionally, spatial resolution of the C−H stretching spectral region has been obtained for the Orion Bar[61] and also for two reflection nebuale.[62] These measurements provide the intensity ratios of the 3.29-μm UIR band to those of the weaker features red of the primary peak as a function of distance away from the H_{II} region and into the molecular cloud. If these weaker bands were the result of anharmonically shifted transitions, one would expect their relative intensities to decrease with decreasing far-UV photon flux into the cloud. Instead, the observations are consistent with the hypothesis that aliphatic functional groups are responsible for these bands.

TABLE 14: Characteristic PAH Bandwidths from UV-LID/SPIRES Experiments

PAH local mode	wavelength range $\lambda_1 - \lambda_2$ (μm)	mean bandwidth all UV-LID PAHs (cm^{-1})	mean bandwidth coronene and perylene (cm^{-1})
C−H stretch	3.1−3.8	52.6	24.3
combinations	5−6	61.7	46.4
C−C stretch	6−8	59.6	33.1
C−H in−plane bend	8−10.8	34.8	23.4
C−H oop bend	10.8−16	34.2	15.2

C. Continuum Emission near 3 μm. Continuum emission between 1 and 5 μm was observed by Sellgren, and fit to a 1000 K blackbody temperature.[44] To explain the 1000 K continuum blackbody emission, Sellgren postulated that this emission comes from nonequilibrium emission from very small grains (fewer than 100 atoms) that are excited by UV photons. This idea was a precursor to the hypothesis that PAHs are responsible for the UIRs.[3,5] The PAH hypothesis, however, has focused on the distinct UIR bands. The observation of continuum emission from benzene photolysis products following multiphoton excitation provides a possible link between PAHs and this continuum emission which is observed in some UIR sources. It is also worth noting that in the spatially resolved spectra of the reflection nebula NGC 1333 SVS3, Joblin and co-workers observe a broad continuum between 3.15 and 3.6 μm, which increases in intensity and extends to shorter wavelengths with decreasing distance from the stellar excitation source.[62]

D. Implications for other PAHs. These experiments unambiguously demonstrate that the proposed mechanism for UIR emission (UV excitation of a polyatomic molecule followed by internal conversion and IR emission) can generate IR emission spectra with band shapes and bandwidths similar to those observed in the UIRs. Although some molecules, especially the smaller PAHs such as naphthalene, phenanthrene, and their substituted analogues, exhibit bandwidths broader than those observed in the UIRs, the larger molecules such as perylene and coronene tend to produce bands with widths somewhat smaller than the widths of corresponding UIR bands.

Although a difference is observed in bandwidth as a function of molecular size, the bandwidth also increases with increasing vibrational energy. Temperature-dependent gas cell observations report a linear dependence in temperature.[20] Comparison of the red shifts of the laser desorbed bands to the gas cell data suggests that the larger desorbed molecules have lower temperatures than the smaller molecules. The temperatures of pyrene and coronene listed in Tables 11 and 12, respectively, compare favorably to the effective temperatures anticipated for larger (ca. 50 C atoms) PAHs in UIR-generating nebulae. Therefore, the observed bandwidths for the largest PAHs studied with the UV-LID experiment are thought to be appropriate for models of the UIR bands. Bandwidths for characteristic PAH vibrational modes that can be used to model UIR emission are listed in Table 14. The values obtained from the two largest PAHs studied here are thought to be more representative of PAHs that could potentially contribute to the UIRs.

VI. Conclusions

UV-LID has been used to produce sufficient quantities of gas-phase PAHs for transient infrared emission spectroscopy using a cryogenic monochromator and a BIB-SSPM detector. An empirically observed temperature-dependent red shift of the prominent bands has been used to estimate vibrational temperatures of ~1000 K for pyrene and ~800 K for coronene. A triangular monochromator-slit function was convoluted with a Lorentzian band-shape function to obtain a functional form that approximates the observed band shapes. The observed bands were fit to this functional form to extract line widths and frequencies of these bands under conditions relevant to the PAH-UIR hypothesis. When all the PAHs that were studied are considered, the observed bandwidths are broader than the widths of the corresponding UIR bands. However, if only the largest PAHs studied are considered, the observed bandwidths are slightly smaller than the corresponding UIR bandwidths.

It is worth noting that the IR emission studies of PAHs with high internal energy have yielded no great spectroscopic surprises. Given empirical data for bandwidths and temperature-dependent red shifts, emission spectra can be reliably calculated (with the exception of the 5−6-μm overtone and combination bands) using ab initio frequencies and intensities; matrix data can also be used. The methodology for such a calculation is presented in another publication;[28] a comparison between experimental and calculated spectra is presented there.

The high internal energy influences the spectra in two ways; the bands are broadened and red-shifted with increasing internal energy. Measurements of the naphthalene 3.3-μm band under different conditions indicate that the broadening introduced by a multitude of anharmonically shifted excited vibrational states dominates the observed bandwidths in the UV-LID experiments.

The PAHs studied here do not produce an exact spectral match to the UIRs. This finding does not contradict, but rather reinforces, established limitations to the PAH-UIR hypothesis. The UV radiation typical of UIR sources favors a population of PAHs that are both ionized[17] and considerably larger than those studied here. For example, Allain, Leach, and Sedlmayr[63,18] find that PAH cations smaller than 50 C atoms (N_C < 50) are not anticipated to be stable when subjected to photon energies common to regions of UIR emission. Additional evidence that PAH cations contribute to the UIRs comes from a study of the spatial variation of the ratio of the 8.6 μm/11.3 μm UIR intensities.[64] The variation in this ratio supports the idea that PAH cations contribute to the UIRs and indicates that the extent of PAH ionization decreases with increasing distance from the exciting star.

To rigorously test the PAH-UIR hypothesis, one would ideally observe emission from such molecules in the gas phase with internal energies up to 13.6 eV. Unfortunately, such a direct test of the PAH-UIR hypothesis is not currently possible. Although accurate calculations for the frequencies and intensities of such molecules also currently defy theory, it is quite probable that future advances in ab initio methods will provide data for a sufficient number of large (N_C > 50) PAH cations to adequately test the PAH-UIR hypothesis. Spectral parameters from PAH emission data presented here and elsewhere,[20] have been used to simulate the emission spectra using frequencies and intensities from ab initio data.[28,32] This approach can be used to simulate UIR emission from larger candidate PAHs, which cannot yet be measured by gas-phase emission methods, when matrix or ab initio data become available.

Acknowledgment. This work was supported by the NASA Astrophysics program, the NASA Exobiology program, and fellowships from the Deutsche Forschungsgemeinschaft (S.S.), the Consiglio Nazionale delle Recerche (Italy) (N.B.), the Miller Institute for Basic Research in Science (J.H.), and the Max-Plank-Gesellschaft and the Alexander von Humboldt Stiftung (B.S.). The authors thank Infrared Laboratories for exemplary long-term support of the cryogenic monochromator. We gratefully acknowledge Rockwell International for use of the detector. The authors thank Dr. John Fetzer and the Chevron Research Company for the sample of benzo[1,2,3-*bc*:4,5,6-*b′c′*]dicoronene.

References and Notes

(1) Allamandola, L. J.; Sandford, S. A.; Hudgins, D. M.; Witteborn, F. C. Airborne and Laboratory Studies of Interstellar PAHs. In *Airborne Astronomy Symposium on the Galactic Ecosystem*; Haas, M. R., Davidson, J. A., Erickson, E. F., Eds.; Astronomical Society of the Pacific: San Francisco, 1995; Vol. 73, pp 23−32.

(2) Allamandola, L. J.; Tielens, A. G. G. M.; Barker, J. R. *Astrophys. J., Suppl. Ser.* **1989**, *71*, 733−775.

(3) Léger, A.; Puget, J. L. *Astron. Astrophys.* **1984**, *137*, L5−L8.

(4) Léger, A.; d'Hendecourt, L. *Ann. Phys. (France)* **1989**, *14*, 181−206.

(5) Allamandola, L. J.; Tielens, A. G. G. M.; Barker, J. R. *Astrophys. J.* **1985**, *290*, L25−L28.

(6) Langhoff, S. R. *J. Phys. Chem.* **1996**, *100*, 2819−2841.

(7) de Frees, D. J.; Miller, M. D.; Talbi, D.; Pauzat, F.; Ellinger, Y. *Astrophys. J.* **1993**, *408*, 530−538.

(8) Hudgins, D. M.; Allamandola, L. J. *J. Phys. Chem.* **1995**, *99*, 3033−3046.

(9) Hudgins, D. M.; Sandford, S. A.; Allamandola, L. J. *J. Phys. Chem.* **1994**, *98*, 4243−4253.

(10) Hudgins, D. M.; Allamandola, L. J. *J. Phys. Chem.* **1995**, *99*, 8978−8986.

(11) Vala, M.; Szczepanski, J.; Pauzat, F.; Parisel, O.; Talbi, D.; Ellinger, Y. *J. Phys. Chem.* **1994**, *98*, 9187−9196.

(12) Szczepanski, J.; Wehlburg, C.; Vala, M. *Chem. Phys. Lett.* **1995**, *232*, 221−228.

(13) Szczepanski, J.; Vala, M.; Talbi, D.; Parisel, O.; Ellinger, Y. *J. Chem. Phys.* **1993**, *98*, 4494−4511.

(14) Szczepanski, J.; Roser, D.; Personette, W.; Eyring, M.; Pellow, R.; Vala, M. *J. Phys. Chem.* **1992**, *96*, 7876−7881.

(15) Szczepanski, J.; Chapo, C.; Vala, M. *Chem. Phys. Lett.* **1993**, *205*, 434−439.

(16) Szczepanski, J.; Vala, M. *Astrophys. J.* **1993**, *414*, 646−655.

(17) Omont, A. *Astron. Astrophys.* **1986**, *164*, 159−178.

(18) Allain, T.; Leach, S.; Sedlmayr, E. *Astron. Astrophys.* **1996**, *305*, 616−630.

(19) Joblin, C.; d'Hendecourt, L.; Léger, A.; Défourneau, D. *Astron. Astrophys.* **1994**, *281*, 923−936.

(20) Joblin, C.; Boissel, P.; Léger, A.; d'Hendecourt, L.; Défourneau, D. *Astron. Astrophys.* **1995**, *299*, 835−846.

(21) Robinson, M. S.; Beegle, L. W.; Wdowiak, T. J. *Planet. Space Sci.* **1995**, *43*, 1293−1296.

(22) Cherchneff, I.; Barker, J. R. *Astrophys. J.* **1989**, *341*, L21−L24.

(23) Brenner, J.; Barker, J. R. *Astrophys. J.* **1992**, *388*, L39−L43.

(24) Williams, R. M.; Leone, S. R. *Astrophys. J.* **1995**, *443*, 675−681.

(25) Shan, J.; Suto, M.; Lee, L. C. *Astrophys. J.* **1991**, *383*, 459−465.

(26) Schlemmer, S.; Cook, D. J.; Harrison, J. A.; Wurfel, B.; Chapman, W.; Saykally, R. J. *Science* **1994**, *265*, 1686−1689.

(27) Cook, D. J.; Schlemmer, S.; Balucani, N.; Wagner, D. R.; Steiner, B.; Saykally, R. J. *Nature* **1996**, *380*, 227−229.

(28) Cook, D. J.; Saykally, R. J. *Astrophys. J.*, in press.

(29) Dereniak, E. L.; Crowe, D. G. *Optical Radiation Detectors*; John Wiley & Sons: New York, 1984.

(30) Petroff, M. D.; Stapelbroek, M. G.; Kleinhans, W. A. *Appl. Phys. Lett.* **1987**, *51*, 406−408.

(31) LaViolette, R. A.; Stapelbroek, M. G. *J. Appl. Phys.* **1988**, *65*, 830−836.

(32) Cook, D. J. Single Photon Infrared Emission Spectroscopy. Ph.D. Dissertation, University of California, Berkeley, 1996.

(33) Smalley, R. E.; Wharton, L.; Levy, D. H. *Acc. Chem. Res* **1977**, *10*, 139−145.

(34) Levy, D. H. *Science* **1981**, *214*, 263−269.

(35) Levy, D. H.; Wharton, L.; Smalley, R. E. Laser Spectroscopy in Supersonic Jets. In *Chemical and Biochemical Applications of Lasers*; Moore, C. B., Ed.; Academic: New York, 1977.

(36) Ambrose, D.; Ewing, M. B.; Ghiassee, N. B.; Ochoa, J. C. S. *J. Chem. Thermodyn.* **1990**, *22*, 589−605.

(37) Barker, J. T. *Z. Phys. Chem.* **1910**, *71*, 235−253.

(38) Hiraya, A.; Shobatake, K. *J. Chem. Phys.* **1991**, *94*, 7700−7706.
(39) Pantos, E.; Philis, J.; Bolovinos, A. *J. Mol. Spectrosc.* **1978**, *72*, 36−42.
(40) Herzberg, G. H. *Infrared and Raman Spectra of Polyatomic Molecules*; van Nostrand: Princeton, 1968.
(41) Wurz, P.; Lykke, K. R. *J. Phys. Chem.* **1992**, *96*, 10129−10139.
(42) Yokoyama, A.; Zhao, X.; Hintsa, E. J.; Continetti, R. E.; Lee, Y. T. *J. Chem. Phys.* **1990**, *92*, 4222−4233.
(43) Yerram, M. L.; Brenner, J. D.; King, K. D.; Barker, J. R. *J. Phys. Chem.* **1990**, *94*, 6341−6350.
(44) Sellgren, K. *Astrophys. J.* **1984**, *277*, 623−633.
(45) Makarov, A. A. Spectra of Transitions in the Vibrational Quasi-continuum of Polyatomic Molecules. In *Laser Spectroscopy of Highly Vibrationally Excited Molecules*; Letokhov, V. S., Ed.; Adam Hilger: New York, 1989; pp 106−177.
(46) *Igor Pro*, 3rd ed.; WaveMetrics, Inc.: Lake Oswego, OR, 1996.
(47) Toselli, B. M.; Barker, J. R. *J. Chem. Phys.* **1992**, *97*, 1809−1817.
(48) Brenner, J. D.; Erinjeri, J. P.; Barker, J. R. *Chem. Phys.* **1993**, *175*, 99−111.
(49) Lenzer, T.; Luther, K. *J. Chem. Phys.* **1996**, *104*, 3391−3394.
(50) Lenzer, T.; Luther, K.; Troe, J.; Gilbert, R. G.; Lim, K. F. *J. Chem. Phys.* **1995**, *103*, 626−641.
(51) Lim, K. F. *J. Chem. Phys.* **1994**, *100*, 7385−7399.
(52) Kohlmaier, G. H.; Rabinovitch, B. S. *J. Chem. Phys.* **1963**, *38*, 1692.
(53) Miller, D. R. Free Jet Sources. In *Atomic and Molecular Beam Methods*; Scoles, G., Ed.; Oxford University Press: New York, 1988; Vol. 1, pp 14−53.
(54) Cohen, M.; Tielens, A. G. G. M.; Bregman, J.; Witteborn, F. C.; Rank, D. M.; Allamandola, L. J.; Wooden, D. H.; de Muizon, M. J. *Astrophys. J.* **1989**, *341*, 246−269.
(55) Cohen, M.; Allamandola, L. J.; Tielens, A. G. G. M.; Bregman, J.; Simpson, J. P.; Witteborn, F. C.; Wooden, D.; Rank, D. *Astrophys. J.* **1986**, *302*, 737−749.
(56) Allamandola, L. J.; Bregman, J. D.; Sandford, S. A.; Tielens, A. G. G. M.; Witteborn, F. C.; Wooden, D. H.; Rank, D. *Astrophys. J.* **1989**, *345*, L59−L62.
(57) Barker, J. R.; Allamandola, L. J.; Tielens, A. G. G. M. *Astrophys. J.* **1987**, *315*, L61−L65.
(58) Bellamy, L. J. *The Infrared Spectra of Complex Molecules*, 3rd ed.; Chapman and Hall Ltd.: London, 1975.
(59) Schutte, W. A.; Tielens, A. G. G. M.; Allamandola, L. J. *Astrophys. J.* **1993**, *415*, 397−414.
(60) Geballe, T. R.; Joblin, C.; d'Hendecourt, L. B.; de Muizon, M. J.; Tielens, A. G. G. M.; Léger, A. *Astrophys. J.* **1994**, *434*, L15−L18.
(61) Sloan, G. C.; Bregman, J. D.; Geballe, T. R.; Allamandola, L. J.; Woodward, C. E. *Astrophys. J.* **1997**, *474*, 735−740.
(62) Joblin, C.; Tielens, A. G. G. M.; Allamandola, L. J.; Geballe, T. R. *Astrophys. J.* **1996**, *458*, 610−620.
(63) Allain, T.; Leach, S.; Sedlmayr, E. *Astron. Astrophys.* **1996**, *305*, 602−615.
(64) Joblin, C.; Tielens, A. G. G. M.; Geballe, T. R.; Wooden, D. H. *Astrophys. J.* **1996**, *460*, L119−L122.
(65) Roche, P. F.; Lucas, P. W.; Hoare, M. G.; Aitken, D. K.; Smith, C. H. *Mon. Not. R. Astron. Soc.* **1996**, *280*, 924−936.